Retrievals of riming and snow density from vertically-pointing Doppler radars

Article

Accepted Version

Retrievals of riming and snow density from vertically-pointing Doppler radars

S. L. Mason[1,2], C. J. Chiu[3], R. J. Hogan[1,4], D. Moisseev[5,6], S. Kneifel[7]

[1]Department of Meteorology, University of Reading, Reading, UK
[2]National Centre for Earth Observation (NCEO), University of Reading, Reading, UK
[3]Colorado State University, Fort Collins, Colorado, USA
[4]European Centre for Medium-range Weather Forecasts (ECMWF), Reading, UK
[5]Institute for Atmospheric and Earth System Research/Physics, Faculty of Science, University of Helsinki, Finland
[6]Finnish Meteorological Institute, Helsinki, Finland
[7]Institute of Geophysics and Meteorology, University of Cologne, Cologne, Germany

Key Points:

- The CAPTIVATE optimal estimation retrieval algorithm is applied to zenith-pointing Doppler cloud radars deployed during the Biogenic Aerosolos—Effects on Clouds and Climate field campaign (BAECC 2014), in Hyytiälä, Finland.
- Doppler velocity is exploited to retrieve a parameter that modulates the mass, area and radar backscatter cross-sections to represent the continuum of particle morphologies from unrimed aggregates to graupel and hail.
- The retrieval provides insights into microphysical processes including aggregation and riming. Retrieved particle density is correlated with the availability of super-cooled liquid water, demonstrating potential to use the retrieval to diagnose embedded layers of mixed-phase clouds.

Corresponding author: S. L. Mason, s.l.mason@reading.ac.uk

Abstract

Retrievals of ice and snow are made from Ka- and W-band zenith-pointing Doppler radars at Hyytiälä, Finland, during the snow experiment (SNEX) component of the Biogenic Aerosols: Effects on Clouds and Climate (BAECC 2014) field campaign. In a novel optimal estimation retrieval, mean Doppler velocity is exploited to retrieve a "density factor" parameter which modulates the mass, shape, terminal velocity and backscatter cross-sections of ice particles. In a case study including aggregate snow and graupel we find that snow rate and ensemble mean ice density can be retrieved to within 50 % of in-situ measurements at the surface using dual-frequency Doppler radar retrievals. While Doppler measurements are essential to the retrieval of particle density, the dual-frequency ratio provides a strong constraint on particle size. The retrieved density factor is strongly correlated with liquid water path, indicating that riming is the primary process by which the density factor is modulated. Using liquid water path as a proxy for riming, profiles classified as unrimed snow, rimed snow and graupel exhibit distinct features characteristic of aggregation and riming processes, suggesting the potential to make estimates of process rates from these retrievals. We discuss the potential application of the technique to future satellite missions.

1 Introduction

Estimates of the global volume and distribution of snow are critical to understanding the atmospheric water budget and surface hydrology. While the first generation of spaceborne cloud and precipitation radars has greatly improved the detection of snow, remote-sensed estimates of snow mass flux and its microphysical properties remain highly uncertain. Understanding the microphysics of snow production within ice clouds is also critical to global rainfall: CloudSat 94-GHz radar [*Stephens et al.*, 2002] observations reveal that 85–90% of all precipitation events in the extratropics and poles originate in the ice phase, and that 34–40% of rain events in the subtropics and tropics fall from melting ice [*Field and Heymsfield*, 2015]. CloudSat snow retrievals [e.g. *Liu*, 2008; *Kulie and Bennartz*, 2009] have enabled the first remote-sensed estimates of snow over remote polar regions [*Palerme et al.*, 2014], and surveys of snow regimes [*Chen et al.*, 2016; *Kulie et al.*, 2016], but further microphysical insights are anticipated from upcoming satellite missions. The first of a second generation of satellite radars is the dual-frequency precipitation radar (DPR) aboard the global precipitation measurement mission [GPM; *Hou et al.*, 2014]; however, initial comparisons suggest DPR detects only about one-third of the mass of snow seen by CloudSat, concen-

trated in the heaviest 5% of snow events [*Casella et al.*, 2017]. Work is ongoing to better evaluate remote-sensed snow rate at the surface [e.g. *Heymsfield et al.*, 2016] with the aim of reducing uncertainties in retrievals from current satellite capability and informing the design of future satellite sensors.

Remote-sensing of ice and snow requires knowledge of the morphology of ice particles, which may be any combination of pristine ice crystals grown by vapour deposition, aggregates or fragments formed from interactions between ice particles, or rimed particles and graupel having collected liquid drops in mixed-phase cloud. While a majority of snow is assumed to fall as aggregate snowflakes [*Langleben*, 1954], the masses and fallspeeds of ice particles remain fundamental to uncertainties in radar retrievals [*Hiley et al.*, 2011]. Ice particle properties are especially uncertain in and below mixed-phase clouds, which are common in the extratropics and poles [*Hogan et al.*, 2003, 2004; *Cesana et al.*, 2012], radiatively important in the polar regions and extratropics [e.g. *Shupe et al.*, 2004], imperfectly detected by spaceborne radar and lidar [e.g. *Ceccaldi et al.*, 2013], and poorly represented in models [e.g. *Tan et al.*, 2016]. Studies at ground stations have attributed 40% or more of the mass of snow to rimed ice [*Harimaya and Sato*, 1989; *Mitchell et al.*, 1990; *Moisseev et al.*, 2017], suggesting large uncertainties in remote-sensed estimates of snow rate while riming goes undiagnosed, and riming has been strongly associated with heavy accumulation events in mountainous regions [*Grazioli et al.*, 2015]. Remote-sensed estimates of snow stand to be improved by the capability to diagnose riming in mixed-phase clouds, hence to better estimate ice particle properties and the mass flux of snow.

Recent ground-based measurement campaigns have facilitated studies of snow microphysics using deployments of advanced radars, lidars and passive remote-sensors co-located with in situ measurements of snow particles [e.g. *Szyrmer and Zawadzki*, 2014; *Petäjä et al.*, 2016]. Combined particle imaging and snow gauge instruments have enabled the quantification of ice bulk density and rime mass [*Tiira et al.*, 2016; *Moisseev et al.*, 2017; *von Lerber et al.*, 2017; *Grazioli et al.*, 2015], building upon previous studies characterising particle morphologies and degrees of riming [e.g. *Harimaya and Sato*, 1989; *Mitchell et al.*, 1990]. These campaigns provide opportunities to evaluate and intercompare the representation of ice and mixed-phase microphysics used in numerical models [*Lin et al.*, 2011; *Morrison and Milbrandt*, 2015; *Morrison et al.*, 2015], as well as of ice particle morphology and growth processes as they relate to radar backscatter [*Kneifel et al.*, 2011; *Leinonen and Szyrmer*, 2015]. Triple-frequency radar measurements have allowed for the evaluation of particle mod-

els using the signatures of rimed and unrimed ice particles [*Kneifel et al.*, 2015; *Stein et al.*, 2015], a technique that has recently been applied to colocated CloudSat and GPM measurements [*Yin et al.*, 2017]. With Doppler radar capability, the morphology of snow can also be inferred from terminal velocities of particles to estimate the degree of riming [*Mosimann*, 1995] or the density of rimed aggregates [*Szyrmer and Zawadzki*, 2014; **?**], and it is possible in some cases to distinguish ice from cloud droplets using Doppler spectra in mixed-phase cloud [*Kalesse et al.*, 2016]. Recent ground-based remote-sensing and in situ measurement campaigns have demonstrated the application of Doppler and multiple-frequency radar observations to improved retrievals of snow and riming.

In this study we demonstrate the novel retrieval of the properties of snow particles using vertically-pointing dual-frequency Doppler radars at Hyytiälä, Finland. Mean Doppler velocity, a measure of the terminal velocity of hydrometeors, is used to estimate a parameter that modulates the properties of ice particles along a continuum from unrimed aggregates to graupel and hail. The retrieval is carried out within the optimal estimation framework for Cloud Aerosol and Precipitation from mulTiple Instruments using a VAriational TEchnique (CAPTIVATE), which provides the flexibility to assimilate observed variables from a range of ground-based instruments. We consider the contribution of Doppler velocity and dual-frequency radar reflectivity measurements to the retrieval, and compare against retrievals in which particle density does not vary. The retrieved snow rate, particle size distribution and bulk density are evaluated against in-situ measurements at the surface. This method for estimating ice particle morphology from mean Doppler velocity should be applicable to the network of ARM and Cloudnet [*Illingworth et al.*, 2007] "supersites" with multi-frequency Doppler radars, as well as to the upcoming ESA/JAXA Earth Cloud Aerosol Radiation Explorer [EarthCARE; *Illingworth et al.*, 2015], which will feature the first spaceborne Doppler cloud radar in synergy with lidar and radiometers. In addition to Doppler capability, spaceborne multiple-frequency cloud radars have long been of interest to further improve global observations of ice clouds and snow [*Hogan and Illingworth*, 1999; *Tanelli et al.*, 2009; *Löhnert et al.*, 2011; *Leinonen and Szyrmer*, 2015; *National Academies of Sciences Engineering and Medicine*, 2018].

The paper is structured as follows: we describe the components of the CAPTIVATE retrieval framework pertinent to estimates of ice and snow from radar measurements, with a focus on formulating a new parameter with which to represent ice particles over a range of densities from unrimed aggregates to graupel and hail (Section 2), and lay out the mea-

surements and atmospheric state data used for the present study (Section 3). We then present the results of retrievals for a case study of a frontal snow event with significant riming (Section 4.1), and a statistical evaluation of a retrieval of 10 snow events over a 2 month observation period (Section 4.2). In our concluding remarks we consider applications of the retrieval to future satellite radar missions (Section 5).

2 Retrieval framework

The CAPTIVATE retrieval framework [*Mason et al.*, 2017] has been developed for radar–lidar–radiometer synergy retrievals from EarthCARE [*Illingworth et al.*, 2015]. CAPTIVATE therefore includes instrument forward-models for the Doppler radar and high-spectral resolution lidar aboard EarthCARE, but is also designed to be easily configurable for active and passive sensors on ground-based and airborne platforms. Here we focus on the retrieval of snow from zenith-pointing ground-based radar measurements. The retrieval of ice and snow builds upon the methods employed for the synergy of CloudSat/CALIPSO observations [*Delanoë and Hogan*, 2008, 2010]; the novelty of the present retrieval is the availability of Doppler velocity measurements.

2.1 Cost function and minimization

The retrieval operates on a column-by-column basis to make an optimal estimate of the vector of state variables $\mathbf{x}$ that best explains the observed variables $\mathbf{y}$ within the bounds of prior expectations and measurement uncertainties [*Rodgers*, 2000]. The optimal estimate is that which minimizes the cost function

$$J = \frac{1}{2}\delta\mathbf{x}^{\mathsf{T}}\mathbf{B}^{-1}\delta\mathbf{x} + \frac{1}{2}\delta\mathbf{y}^{\mathsf{T}}\mathbf{R}^{-1}\delta\mathbf{y} + J_c\left(\mathbf{x}\right), \tag{1}$$

where $\delta\mathbf{x} = \mathbf{x} - \mathbf{x}_a$ is the difference between the state vector and its prior, and $\mathbf{B}$ the error covariance matrix of the priors; $\delta\mathbf{y} = \mathbf{y} - H\left(\mathbf{x}\right)$ is the difference between the observed variables and the forward-modelled observations $H(\mathbf{x})$, and $\mathbf{R}$ the error covariances of the observations and forward models; and $J_c\left(\mathbf{x}\right)$ optionally applies regularization constraints to the vertical profile of the state vector [*Twomey*, 1977]. By quantifying uncertainties in the prior estimates of the state, measurement errors, and uncertainties in the implementation of the forward-models, the retrieval yields a robust best-estimate of the state variables and their associated error uncertainties. The cost function is minimized by iterating on the state vector from the prior in the direction of the first and second derivatives of the cost function [the

Levenberg-Marquadt method; *Rodgers*, 2000]. The derivatives are computed efficiently and transparently using the combined array and automatic differentiation C++ software library, Adept [*Hogan*, 2014, 2017].

The vectors of state variables through the vertical profile $\mathbf{x}_i$ for n classes of hydrometeor are retrieved from the observed variables $\mathbf{y}_j$ of m instruments:

$$\mathbf{x} = \begin{pmatrix} \mathbf{x}_1 \\ \mathbf{x}_2 \\ \vdots \\ \mathbf{x}_n \end{pmatrix}, \qquad \mathbf{y} = \begin{pmatrix} \mathbf{y}_1 \\ \mathbf{y}_2 \\ \vdots \\ \mathbf{y}_m \end{pmatrix}.$$

Both the selection of appropriate state variables for ice particles (Section 2.3) and the formulation of a radar forward-model for the observed variables (Section 2.4) depend on an underlying physical representation of ice particles: their size distribution, shape and mass, and their terminal fallspeeds.

2.2 Representation of ice particle properties

The bulk quantities of primary interest for remote-sensing are related to integrals over the particle size distribution (PSD; $N(D)$) with the average properties of ice particles, as a function of maximum particle dimension D. Unless stated otherwise, SI units are used. The ice water content (IWC) requires the mass of ice particles, $m(D)$:

$$IWC = \int_0^\infty m(D)\, N(D)\, dD, \tag{2}$$

while the mass flux or snow rate also includes particle terminal velocities, $v(D)$:

$$S = \int_0^\infty v(D)\, m(D)\, N(D)\, dD. \tag{3}$$

A characteristic bulk density of ice particles can be calculated as a volume flux-weighted density:

$$\overline{\rho} = \frac{\int_0^\infty m(D)\, v(D)\, N(D)\, dD}{\frac{\pi}{6} AR \int_0^\infty D^3\, v(D)\, N(D)\, dD} \tag{4}$$

where AR is the aspect ratio of a horizontally-aligned oblate spheroid enclosing the particle. A volume flux-weighted density for ease of comparison with estimates derived from in situ measurements of accumulation with a snow gauge [e.g. *Moisseev et al.*, 2017; *von Lerber et al.*, 2017]. While integrated quantities such as snow rate are especially sensitive to the formulation of the mass-size relation [*Heymsfield et al.*, 2010; *Delanoë et al.*, 2014], in

this study it will also be important to relate the mass and shape of particles to their terminal velocity in order to retrieve the morphology of snow particles from Doppler radar measurements.

In the following sections we first describe the PSD (Section 2.2.1), then the mass-size (Section 2.2.2) and area-size (Section 2.2.3) relations for a range of ice particles, and finally how particle properties are combined to estimate terminal fallspeeds (Section 2.2.4).

2.2.1 Particle size distribution

The PSD is represented as a normalized spectrum of the form

$$N(D) = N_w F\left(D/D_0\right). \tag{5}$$

where N_w is the normalized number concentration, D_0 is the median volume diameter [*Testud et al.*, 2001], and the function $F(D/D_0)$ can be either that of the normalized gamma distribution [*Testud et al.*, 2001; *Illingworth and Blackman*, 2002; *Delanoë et al.*, 2005], or the universal modified gamma distribution derived by *Field et al.* [2005] for extratropical ice clouds [see also *Field et al.*, 2007; *Delanoë and Hogan*, 2008]. The normalized number concentration can be estimated from the moments of the PSD:

$$N_w = M_2^4/M_3^3 \tag{6}$$

where M_n is the n^{th} moment. When using the gamma function a constant shape parameter of $\mu = 2$ is assumed in order to simplify the representation of the PSD; the shape parameter makes the smallest contribution to uncertainties in the retrieved ice water content [*Delanoë et al.*, 2005]. In practice for the present study, the differences between the retrieved quantities using the normalized gamma and *Field et al.* [2005] PSD were found to be within the uncertainty of the retrievals; in the results presented here the *Field et al.* [2005] PSD is used unless otherwise stated.

2.2.2 Mass-size relations

Ice particle mass is expressed as a function of maximum dimension by the power law

$$m(D) = a_m D^{b_m}, \tag{7}$$

where the prefactor a_m scales the density of ice at all sizes, and the exponent b_m controls the size-dependence of particle mass and is related to the particle growth mechanism or shape

of the particle. Aggregate snowflakes have exponents around $b_m = 2$, close to the theoretical value for fractals [*Westbrook et al.*, 2004; *Stein et al.*, 2015]. More rounded graupel and hail particles have exponents closer to $b_m = 3$, the physical maximum for spheres [*Leinonen and Moisseev*, 2015].

While snow particles are observed to vary greatly in morphology, the majority of snow is thought to fall as aggregate snowflakes [*Langleben*, 1954]—indeed, the mass-size relations used for ice and snow tend to be derived from measurements dominated by unrimed aggregates. We follow the approach of *Hogan et al.* [2012], who showed that in-situ measurements of cirrus were consistent with radar reflectivities when the mass-size relation derived for "aggregates of unrimed bullets, columns and side-planes" by *Brown and Francis* [1995] was used. In this representation the smallest particles are assumed to be solid quasi-spheroidal ice crystals, while larger aggregates occupy the volume of a horizontally-aligned oblate spheroid with an aspect ratio—that between the minimum (vertical) dimension and the maximum (horizontal) dimension—of $AR = 0.6$. *Hogan et al.* [2012] found that this value provided a good fit to a database of aircraft measurements as well as other studies in the literature. Combining dual-polarization weather radar and surface based snowfall measurements at Hyytiälä, [*Li et al.*, 2018] found that the aspect ratio varies with riming fraction between 0.4 and 0.9, while analysis of PIP images by *Tiira et al.* [2016] yielded a median aspect ratio of 0.72. However, the applicability of particle images to derive particle geometrical properties was questioned by *Jiang et al.* [2017]; hence, *Tiira et al.* [2016] also used a single aspect ratio value of 0.6 for density retrievals. In the present study it was found that assuming $AR = 0.8$ instead of $AR = 0.6$ led to an increase in retrieved ice water content of approximately 20 %, demonstrating that the shape and orientation of ice particles is an important uncertainty in the remote-sensing of snow [see also *Hogan and Westbrook*, 2014].

How does riming affect the mass-size relation of snow? Numerical analogues for "ballistic" collisions between ice particles (aggregation) and between ice particles and supercooled liquid drops (riming) suggest that aggregating particles will retain mass-size exponents around $b_m = 2$, while those growing by riming will tend toward exponents of $b_m = 3$ [*Jullien*, 1992]. A conceptual model for riming introduced by *Heymsfield* [1982] proposes a two stage process for the riming of aggregate snowflakes [see also *Morrison and Milbrandt*, 2015; *Moisseev et al.*, 2017], in which an aggregate is first "filled in" by freezing supercooled drops, increasing the mass of the particle but not its size: this increases the prefactor of the mass-size relation while the exponent remains close to $b_m = 2$ [e.g. *Szyrmer and Zawadzki*,

2014; *Morrison and Milbrandt*, 2015; *Moisseev et al.*, 2017; *von Lerber et al.*, 2017]. That the first stage of riming does not scale the exponent of the mass-size relation is consistent with earlier studies of rimed snow [e.g. *Harimaya and Sato*, 1989; *Mitchell et al.*, 1990]. Once the particle geometry is closed by in-filling, it is classified as graupel. In this second stage rime is accreted to the outside of the particle, adding to both its mass and diameter, and as the particles become rounder in shape the exponent approaches $b_m = 3$ [*Mitchell*, 1996]. The morphology of an ice particle encodes a history of multiple and interacting processes, including aggregation and transitions between stages of riming, which may be observed microscopically [*Fujiyoshi and Wakahama*, 1985] or tracked within a microphysical parameterization scheme [*Morrison et al.*, 2015; *Morrison and Milbrandt*, 2015], but are unlikely to be instantaneously grasped by remote sensing. In a modelling study *Leinonen and Szyrmer* [2015] compared particles that have grown first by aggregation then riming to those that have grown by simultaneous aggregation and riming. While it was found that aggregation and riming, whether in series or in parallel, form particles that are indistinguishable in terms of radar backscatter—an important result for remote-sensing—the corresponding mass-size relations were distinct: when riming followed aggregation the exponent was found to remain close to $b_m = 2.1$ until a relatively high degree of riming; but when riming and aggregation were simultaneous the exponent varied significantly even at low degrees of riming. This complicates the two-stage conceptual model of riming. While we may attempt to formulate a representation of the range of morphologies and densities of ice particles for remote-sensing applications, the possibility of multiple interacting ice processes means we should be cautious about attributing all variations in particle density to riming.

It has been observed that the mass-size relations derived from studies of snow and ice form a continuum of ice particles from unrimed snowflakes to graupel and hail [*Lin and Colle*, 2011]; Fig. 1 shows the mass-size prefactors and exponents a_m and b_m in cgs units and converted where necessary into terms of maximum particle dimension D. Particles with low mass-size prefactors and exponents—in the lower left part of the diagram—include a range of unrimed aggregates, as well as other low-density species such as dendrites, needles and columns. Measurements of unrimed snow from ground-based studies [*Tiira et al.*, 2016; *von Lerber et al.*, 2017] are consistent with aircraft studies of ice clouds [*Heymsfield and Westbrook*, 2010; *Brown and Francis*, 1995], with b_m varying between 1.9 and 2.1. Larger mass-size prefactors and exponents—in the centre to the upper-right part of the diagram—include denser or more compact particles of various kinds, often with some degree of rim-

ing. Exponents for rimed aggregates and low-density graupel are between 2.1 and 2.4 [*Erfani and Mitchell*, 2017; *von Lerber et al.*, 2017]; while for lump graupel and hail classifications [*Mitchell*, 1996; *Mace and Benson*, 2017; *Zikmunda and Vali*, 1972] the exponent approaches 3.0. We note that the position on the mass-size relation diagram is not solely related to the effect of riming, especially for slender 1- and 2-dimensional species such as columns and dendrites: for example, the rimed dendrites in *Erfani and Mitchell* [2017] have a lower mass-size exponent than the unrimed dendrites; and the different sizes of hexagonal columns in *Mitchell* [1996] range from the upper-right part of the diagram for the smallest columns, to the extreme lower-left for the largest.

Variations in ice particle density have been parameterized in many ways. Fixed densities can be assumed depending on the cloud type, with low-density aggregates in stratiform cloud and graupel-like particles in convective cloud [e.g. *Grecu et al.*, 2016]. *Lin et al.* [2011] parameterize ice density according to temperature. *Szyrmer and Zawadzki* [2014] demonstrate a radar retrieval of lightly rimed snow from ground-based dual-frequency Doppler radars in which the prefactor a_m is scaled to increase the density of ice due to riming, while the exponent is fixed at $b_m = 2$. Similarly, *Moisseev et al.* [2017] represented the density of snow by scaling the prefactor of the mass-size relation and holding the exponent constant.

In order to represent a continuum of ice particles from unrimed and rimed aggregates to graupel and hail, we parameterize particle mass based on a “density factor" r (grey line in Fig. 1) that is continuous between the mass-size relation for the unrimed aggregates of *Brown and Francis* [1995] ($m = 0.0121\, D^{1.9}$ kg where $r = 0$) and that of oblate spheroids of solid ice ($m = 288\, D^3$ kg at $r = 1$). The parameterized exponent varies linearly with density factor between these two reference points ($b_m = 1.9$ and $b_m = 3$):

$$b'_m(r) = 3r + 1.9(1 - r), \tag{8}$$

while the prefactor is scaled according to the requirement that particle masses are equivalent for all r at some critical diameter D_c, which can be calculated as $(0.0121/288)^{1/(3-1.9)} = 105\ \mu$m, similar to the transition from quasi-spheroids to aggregates in *Hogan et al.* [2012]. Normalizing by the critical diameter, the mass-size relation for all particles can be expressed

$$m(D, r) = a'_m \left(\frac{D}{D_c}\right)^{b'_m}, \tag{9}$$

where the normalized prefactor $a'_m = a_m D_c^{b_m} = 33.3\ \mu$g is the particle mass at the critical diameter. A similar normalized mass-size relation was employed in *Szyrmer and Zawadzki*

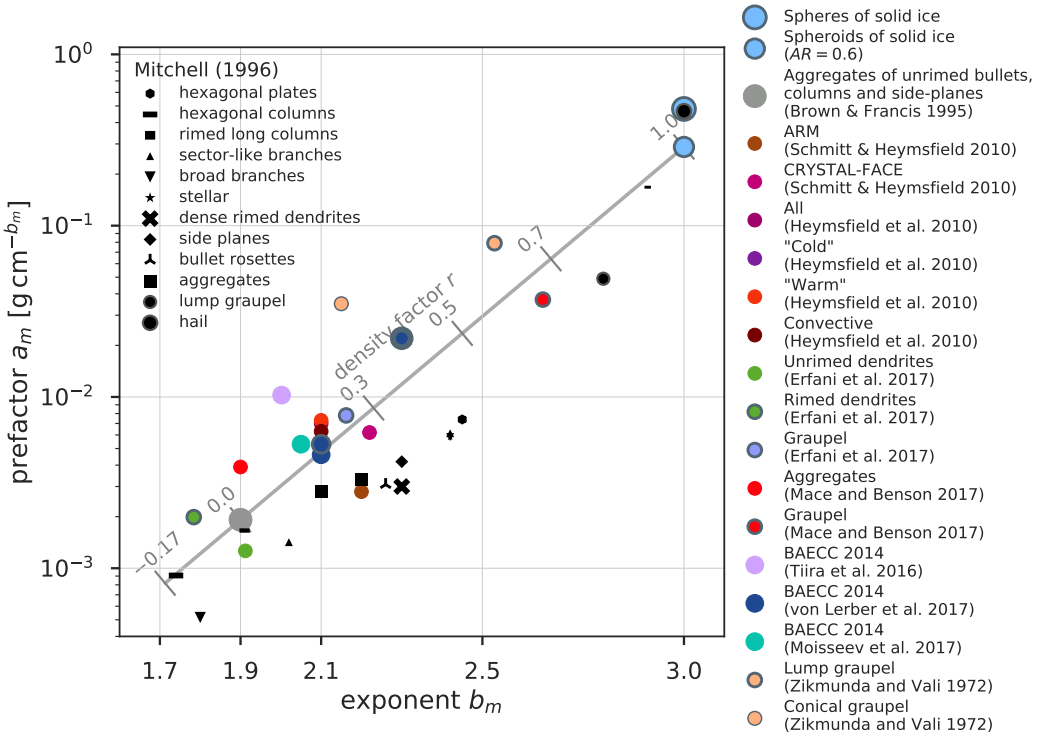

Figure 1. A comparison of $m(D)$ power-law prefactors and exponents. Coloured circles show a_m, b_m for various studies of ice and snow. Black markers correspond to particle types summarized in *Mitchell* [1996]; where multiple markers of a particular type are shown, their relative size indicates the size range for which the mass-size relation was derived. Unrimed aggregates [*Brown and Francis*, 1995] and spheroids of solid ice define the mass-size relation as a function of density factor r: the grey line indicates the values of a_m, b_m parameterized by the density factor in the range $-0.17 < r < 1.0$.

[2014] [see also *Maahn et al.*, 2015; *Maahn and Löhnert*, 2017], but in that study the critical diameter was selected to be close to the median particle diameter to minimize the effect of fixing the exponent of the mass-size relation $b_m = 2$. In the present retrieval all particles smaller than the critical diameter are assumed to be solid quasi-spheroids; expressed another way, the fractional volume of a particle occupied by ice is given by the ice fraction,

$$f(D, r) = \begin{cases} 1.0 & D \leq D_\mathrm{c} \\ (D/D_\mathrm{c})^{b'_\mathrm{m}-3} & D > D_\mathrm{c} \end{cases} \tag{10}$$

The ice fraction-size relation for a range of density factors is shown in Fig. 3.

In terms of the density factor, the unrimed and lightly-rimed snow correspond to low values ($r < 0.3$), and heavily-rimed snow and graupel [*von Lerber et al.*, 2017; *Mace and Benson*, 2017] relate to higher values ($0.3 < r < 0.7$). While $r = 1$ is the upper limit, small negative density factors are possible, and allow for the representation of particles with lower densities such as dendrites [*Erfani and Mitchell*, 2017] or large hexagonal columns [*Mitchell*, 1996].

We note that the density factor is not intended to explicitly represent the effect of the riming process on the mass of a particle, but allows for a smooth transition between unrimed and rimed aggregates to graupel and hail which we hope will be sufficient to allow an estimate of ice morphology based on particle fallspeeds. The density factor pivots the mass-size relation of ice particles larger than the critical diameter (Fig. 3), but without representing the transition features that would corresponding to the multiple stages of riming. A more process-oriented parameterisation of the "in-filling" stage of rimed aggregate snowflakes would be to scale the mass-size prefactor with the density factor, while the exponent remains constant. While this would better represent the conceptual model of the riming process, it would not encompass the observed variability in the mass-size relations of unrimed snowflakes, or the transition to graupel-like particles. A comparison of the two parameterisations indicated that the retrieval was not strongly sensitive to the representation of the density factor, especially for estimates of unrimed to moderately rimed aggregates. With additional observational evidence, a more complex representation of the effects of riming on particle morphology—including expected changes in the masses and shapes of particles during different stages of riming—may allow for improved retrievals and better quantified uncertainties. This should be the subject of future work.

2.2.3 Area-size relation

Similar to the mass-size relation, the cross-sectional area of ice particles is expressed as a power law:

$$A = a_A D^{b_A}. \tag{11}$$

The area-size relation of unrimed aggregates is derived from the mass-size [*Brown and Francis*, 1995] and mass-area relations [*Francis et al.*, 1998] from aircraft measurements of cirrus clouds $A = 0.02038\, D^{1.624}\ \mathrm{m}^2$ in SI units and in terms of maximum dimension. The geometric upper limit for horizontally-aligned oblate spheroids with maximum dimension on the horizontal plane is $A = \pi/4\, D^2\ \mathrm{m}^2$. A comparison of area-size relations from a range of studies (Fig. 2) again shows a relationship between the prefactors and exponents across particle types: lower density factors are consistent with unrimed ice particles [*Schmitt and Heymsfield*, 2010; *Mace and Benson*, 2017], and larger density factors with rimed particles [*Heymsfield and Kajikawa*, 1987], graupel and hail [*Mitchell*, 1996]. While increases in cross-sectional area are consistent with the conceptual model of riming leading to the infilling of aggregates and a transition to rounded graupel-like particles, there is significant variability between particle types: for example, columns may retain low cross-sectional areas despite riming, while riming may have little effect on the cross-sectional area of plates.

To represent the increased cross-sectional area of rimed aggregates and graupel, we scale the area-size relation by the density factor r; however, to represent the more rounded shapes of heavily rimed aggregates and graupel, the cross-sectional area is maximized for $r = r_{\max}$, so that

$$b'_A = 2\frac{r}{r_{\max}} + 1.624\left(1 - \frac{r}{r_{\max}}\right). \tag{12}$$

The prefactor is scaled by a critical diameter D_{c_A}, the size at which the cross-sectional area of unrimed aggregates and spheres are equal, which can be calculated to be 61 μm. The normalized area-size relation is therefore

$$A = a'_A \left(\frac{D}{D_{c_A}}\right)^{b'_A} \tag{13}$$

where the modified prefactor is the area at the critical diameter $a'_A = a_A D_{c_A}^{b'_A}$. Most rimed and unrimed aggregates correspond to density factors $r < 0.3$, while quasi-spheroidal and heavily rimed particles, graupel and hail have $r \approx r_{\max}$. A marginally more complex area-size relation that better fits the observations would be to allow both the prefactor and exponent to vary for $r < r_{\max}$, before scaling only the prefactor up to $r = 1$.

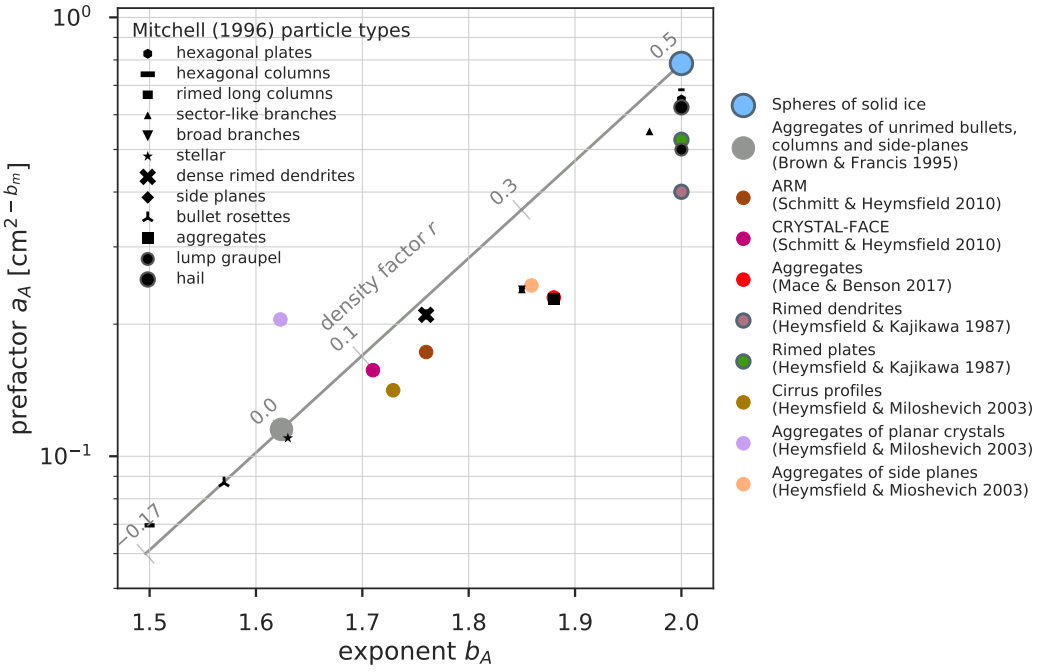

Figure 2. A comparison of power law prefactors and exponents for ice particle area-size relations. Coloured circles show a_A, b_A derived from a range of aircraft and surface studies. Black markers correspond to specific particle types summarized in *Mitchell* [1996]. The parameterized area-size relation, which varies with density factor between unrimed aggregates [$r = 0$ *Brown and Francis*, 1995; *Francis et al.*, 1998] and spheres of solid ice ($r = r_{\max}$), is shown with a grey line.

Particle area is often expressed as the area ratio, which is the cross-sectional area of the particle normalized by area of the circumscribing circle, or

$$A_r(D) = \begin{cases} 1.0 & D \leq D_{c_A} \\ (D/D_{c_A})^{b'_A - 2} & D > D_{c_A} \end{cases}. \tag{14}$$

2.2.4 Velocity-size relation

The boundary layer or hydrodynamic method provides an estimate of the terminal velocity of a hydrometeor based on size, area ratio and mass [e.g. *Mitchell*, 1996; *Mitchell and Heymsfield*, 2005; *Khvorostyanov and Curry*, 2005; *Heymsfield and Westbrook*, 2010] or conversely, an estimate of particle mass from measured diameter, cross-sectional area and fallspeed [e.g. *von Lerber et al.*, 2017]. In the previous sections the mass- and area-size relations for ice particles were expressed as functions of diameter and density factor; hence a look-up table for particle terminal velocities is produced using the method of *Heymsfield and Westbrook* [2010].

The terminal fallspeed of ice particles $v(D, f)$ for a range of maximum dimensions and ice fractions (see eq. 10) is overlaid with curves corresponding to the mass-size relations for a range of density factors (Fig. 3). As the mean Doppler velocity relates to the reflectivity-weighted average of particle fallspeeds, the density factor has the greatest effect on the fallspeeds of the largest particles. While the largest unrimed aggregates do not exceed terminal velocities of $2\,\mathrm{m\,s^{-1}}$, even low density factors effect significant increases in fallspeed for particles of the same size.

2.3 State variables

2.3.1 Extinction coefficient and primed number concentration

The choice of retrieved state variables is flexible within CAPTIVATE, as are any vertical or temporal smoothing applied to the state variables. In this retrieval, a state variable related to the density factor is added to those used for retrievals of ice clouds from radar–lidar synergy described in *Delanoë and Hogan* [2008, 2010]. The first state variable is the visible extinction coefficient of ice in the geometric optics approximation, α_v. The second state variable is the primed number concentration,

$$N'_0 = N_w \alpha_v^{-0.6} \tag{15}$$

from which the normalized number concentration N_w from (5) can be recovered, since the extinction coefficient is also retrieved. *Delanoë and Hogan* [2008] showed using in situ aircraft data that this choice of state variables for ice allows for a convenient a priori estimation of the primed number concentration as a function of atmospheric temperature (Table. 1). An additional parameter, the lidar extinction-to-backscatter ratio, can also be retrieved in radar-lidar synergy applications; however, in this study we assume this variable is constant.

The minimization scheme does not limit the values of retrieved variables, so we formulate state variables such that they remain physically meaningful at all values; this is achieved by using the natural logarithms of N_0' and α_v.

While these choices of state variables for ice and snow are convenient for the reasons described above, they are not necessarily the most physically meaningful quantities. For comparison with in situ measurements, an integrated quantity such as the melted-equivalent snow rate, as well as the median diameter and normalized number concentration, are more convenient. As the extinction coefficient is an integral over the PSD and the primed number concentration relates to a parameter of the PSD by (15), the two state variables are sufficient to calculate the PSD.

2.3.2 Density index

The natural logarithm of the density factor is not a suitable state vector; the density factor should not exceed $r = 1$, but small negative values are physically meaningful. Instead we retrieve the density index r', a state variable defined such that:

$$r = \frac{f(r' + r_0) + f(r_0)}{1 - f(r_0)}, \tag{16}$$

where

$$f(x) = \frac{1}{2} + \frac{\tan^{-1} x}{\pi} \tag{17}$$

and $r_0 = -2$. This transform function has the property that $r = 0$ when $r' = 0$, and for any value of r', r is within the range -0.173 to 1.0. The transform is illustrated in Fig. 4.

2.3.3 Representation of the state vector

To reduce the effect of measurement noise on the retrieval, the profile of each state variable is represented as the basis functions of a cubic spline [*Hogan*, 2007]. The degrees of freedom of the retrieval can therefore be controlled by altering the spacing of the basis func-

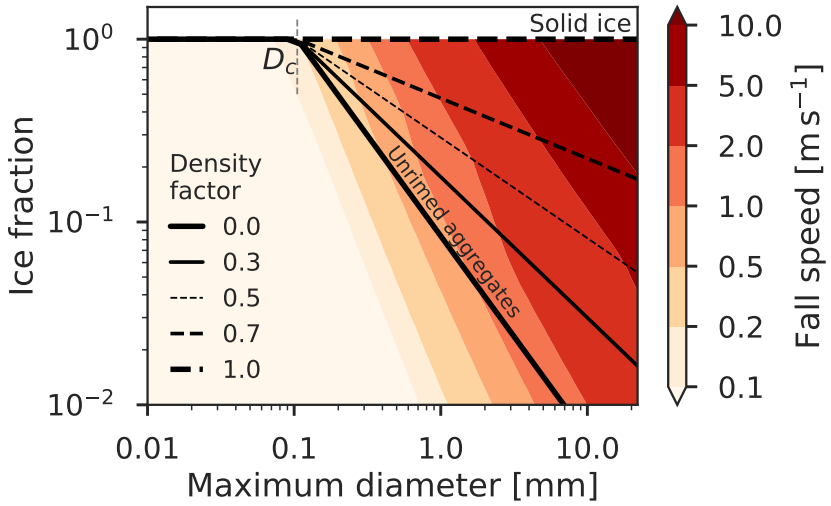

368 **Figure 3.** The terminal fallspeeds $v(D, f)$ of ice particles as a function of maximum dimension D, and
369 ice fraction f. Black lines correspond to the parameterized mass-size relations for density factors between
370 unrimed aggregates ($r = 0$) and spheroids of solid ice ($r = 1$). D_c is the diameter below which all particles
371 are represented as dense quasi-spheroidal particles.

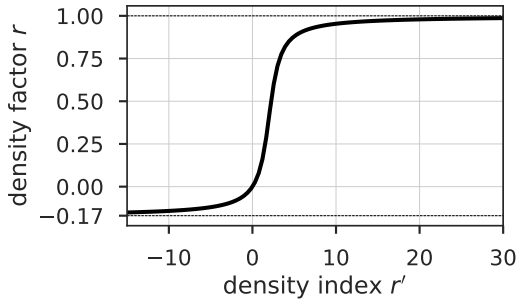

410 **Figure 4.** The transform function between density index r', the retrieved state variable, and the density
411 factor which modulates the particle properties between unrimed aggregates at $r = 0$ and spheroids of solid ice
412 at $r = 1$.

tions, which modifies the effective scales over which features are retrieved [*Rodgers*, 2000]. A Kalman smoother [*Rodgers*, 2000] is applied to the extinction coefficient and density index, so that the retrieval of these quantities is constrained by adjacent profiles. In the first pass of the smoother the retrieval is constrained by subsequent rays and, on the second pass, in both directions. For the retrieval of the density factor, this will have the effect of filtering out smaller-scale fluctuations in the mean Doppler velocity due to turbulent vertical air motion.

The state vector for ice cloud and snow is therefore

$$\mathbf{x}_{\text{ice}} = \begin{pmatrix} \ln \alpha_{\text{v}} \\ \ln N_0' \\ r' \end{pmatrix}.$$

The prior estimate of the state vector and associated uncertainties represent our knowledge of the state before the measurement vector is assimilated. The values and uncertainties of the priors, and the vertical representation of each state variable are summarized in Table 1; note that the uncertainties in the priors are in terms of the natural logarithm of the physical parameters. From a large database of in situ measurements of ice clouds [*Delanoë et al.*, 2005] an expression has been derived for $\ln N_0'$ as a function of atmospheric temperature, with a variance of 1.0 [Fig. 3b in *Delanoë and Hogan*, 2008], and a similar function of temperature is used for the prior extinction coefficient. When fewer observational variables are used it may be necessary to reduce the number of degrees of freedom by holding some state variables at their a priori values; these state variables can be represented within the retrieval as a "model" variable, wherein its value does not vary but its prior uncertainty is assimilated.

2.4 Observed variables and radar forward model

2.4.1 Reflectivity factor

The observed variables for each radar are the apparent radar reflectivity factor Z_f and mean Doppler velocity V_f at the radar frequency f. The reflectivity factor is given by

$$Z_f = 10^{18} \frac{\lambda^4}{\pi^5 |K_f|^2} \int_0^\infty \sigma_f(D)\, N(D)\, dD \tag{18}$$

where λ is the radar wavelength, K_f is the dielectric factor, and $\sigma_f(D)$ is the radar backscatter cross-section. Radar attenuation due to atmospheric gases is modelled from the atmospheric state using *Liebe* [1985], so that this effect is included in the observed and forward-modelled radar reflectivities.

435 **Table 1.** State variables for ice and snow, their priors, uncertainties and vertical representation. Note that
436 we take as the state variables the natural logarithms of key parameters; stated uncertainties are therefore
437 uncertainties in the natural logarithm of the priors.

State variable $\mathbf{x}_i$	Prior $\mathbf{x}_i^a$	Prior uncertainty $\sigma(\mathbf{x}_i^a)$	Cubic spline spacing [m]
Extinction coefficient $\ln \alpha_v$	$-9.2103 - 0.03148\,T$ (where T is in $^\circ C$)	10.0	150
Primed number concentration $\ln N_0'$	$23.03 - 0.12997\,T$ (where T is in $^\circ C$)	1.0	600
Density index r'	0.0	1.0	150

446 Attenuation due to liquid water can be significant for millimetre-wavelength radars,
447 and can either be accounted for by simultaneously retrieving the liquid water content, or by
448 correcting for attenuation in the radar reflectivities prior to the retrieval. The former option
449 is most suited to a radar–lidar–radiometer retrieval wherein the lidar backscatter and a visible
450 radiance may provide adequate constraints; for a radar-only retrieval the available observed
451 variables are dominated by ice, and the retrieval of liquid water content would be undercon-
452 strained. Radar reflectivities can be pre-corrected for liquid attenuation based on an esti-
453 mate of the liquid water path, such as from a microwave radiometer. In this study we follow
454 the correction described in *Kneifel et al.* [2015]; the vertical distribution of SLW not being
455 known, it is distributed evenly over the lowest 4 km of the atmosphere. Alternative correc-
456 tions may be made by assuming all of the attenuation takes place below the lowest radar gate,
457 or by locating the liquid in one or more shallow layers based on other evidence such as a re-
458 cent sounding, or Doppler spectra [e.g. *Kalesse et al.*, 2016]. In practice we found that the
459 uncertainty in W-band radar reflectivity between the different corrections was on the order
460 of 1 to 2 dB; this can be accounted for within CAPTIVATE by increasing the observational
461 uncertainty applied to the measurement vector (see Section. 2.4.4).

462 Reflectivity enhancement due to radar multiple scattering can be modelled using the
463 method of *Hogan* [2008]; however, in this application with ground-based narrow beamwidth
464 radars, we assume multiple scattering is negligible. The uncertainty in the radar reflectivity
465 includes both observational and forward-model errors.

2.4.2 Mean Doppler velocity

Mean Doppler velocity is the reflectivity-weighted fallspeed of hydrometeors

$$V_f = \frac{\int_0^\infty v(D)\,\sigma_f(D)\,N(D)\,dD}{\int_0^\infty \sigma_f(D)\,N(D)\,dD}, \tag{19}$$

where $v(D)$ is corrected for air density, and positive values of mean Doppler velocity are toward the surface. The forward-modelled mean Doppler velocity neglects air motion, the effects of which are also included in the observational uncertainty. In the stratiform snow events in this study we assume that the mean Doppler velocity is dominated by the terminal velocities of hydrometeors rather than vertical air motions. In convective situations or where ice particles are very small, this assumption may not be justified, and would lead to a misdiagnosis of particle density; this will be considered in Section 4.1.

2.4.3 Scattering models

In addition to the density and shape of snow particles (Section 2.2), variability in particle morphology has a significant impact on the scattering of microwave radiation, which must be approximated within the radar forward-model. The self-similar Rayleigh-Gans approximation [SSRGA; *Hogan and Westbrook*, 2014; *Hogan et al.*, 2017] provides an accurate estimate of the radar backscatter cross-section for unrimed aggregates, but underestimates the radar backscatter of higher-density rimed particles. Snow particles have often been approximated by "soft spheroids"—oblate spheroids composed of a homogenous mixture of ice and air—for which the radar backscatter can be estimated using the **T**-matrix method [e.g. *Hogan et al.*, 2012]. *Leinonen and Szyrmer* [2015] found that soft spheroids provide a good approximation to the backscatter of dense graupel-like particles, but not to rimed aggregates. In both approximations particles are represented as occupying the volume of horizontally-aligned oblate spheroids with an aspect ratio of $AR = 0.6$ [*Hogan et al.*, 2012].

In the absence of an explicit model for rimed aggregates, we represent the backscatter cross-section in the transition from unrimed aggregates to graupel as an external mixture between SSRGA ($r \leq 0.2$) and soft spheroids ($r \geq 0.5$). These thresholds were selected based on the ranges of density factors associated with mass-size relations for studies of unrimed aggregates and graupel (Fig. 1). As a check on this representation, the forward-modelled radar backscatter from a gamma distribution of particles was used to generate dual-wavelength ratios (DWRs) at Ka–W-bands and X–Ka-bands for a range of density factors (Fig. 5); these curves are overlaid with triple-frequency radar measurements from three snow events during

BAECC 2014 [*Kneifel et al.*, 2015, c.f. their Fig. 1]. A thin contour highlights the most frequent DWRs observed during the snow event that is studied in Section 4.1. The upright band of $DWR_{\mathrm{Ka-W}} < 10\,\mathrm{dB}$ and large $DWR_{\mathrm{X-Ka}}$ corresponds to the "hook" feature identified for unrimed aggregates, while the flat feature with low $DWR_{\mathrm{X-Ka}}$ is associated with denser graupel-like particles. The triple-frequency signatures represented by SSRGA ($r \leq 0.2$) resemble those of unrimed aggregates, while the soft spheroids ($r \geq 0.5$) fit the flatter signature associated with graupel. This demonstrates that a simple hybrid representation at least qualitatively permits the signatures of unrimed aggregates and dense rimed particles in multiple-frequency radar observations—but does not necessarily address known limitations in the soft spheroid approximation for a range of dense particles [*Leinonen and Szyrmer*, 2015; *Hogan et al.*, 2017]. The modelling and measurement of the morphology and multiple-frequency radar scattering of ice particles are of significant research interest [e.g. *Kneifel et al.*, 2018], and improved approximations for the backscatter cross-sections for rimed aggregates will both reduce uncertainties in the present retrieval, and allow for increased confidence in multiple-frequency radar retrievals of snow.

2.4.4 Measurement vector

The vector of observed variables for a dual-frequency Doppler radar retrieval is

$$\mathbf{y} = \begin{pmatrix} Z_{\mathrm{f}_0} \\ V_{\mathrm{f}_0} \\ Z_{\mathrm{f}_1} \\ V_{\mathrm{f}_1} \end{pmatrix}.$$

In principal more than two radar frequencies could be included in the measurement vector; and in practice, as discussed in the next section, some of the observed variables may not be assimilated in the present study.

The uncertainties in the measurement vector includes the stated measurement error for the instruments (Table 2), other sources of observational uncertainty, and an estimate of the uncertainties in the assumptions that form the basis of the instrument forward-model. For a retrieval that relies upon the mean Doppler velocity to estimate the properties of hydrometeors, the treatment of and sensitivity to uncertainties in Doppler measurements are of particular interest. For the present study we assume uncertainties of 3 dB in the radar reflectivities and $1.0\,\mathrm{m\,s^{-1}}$ in the mean Doppler velocity.

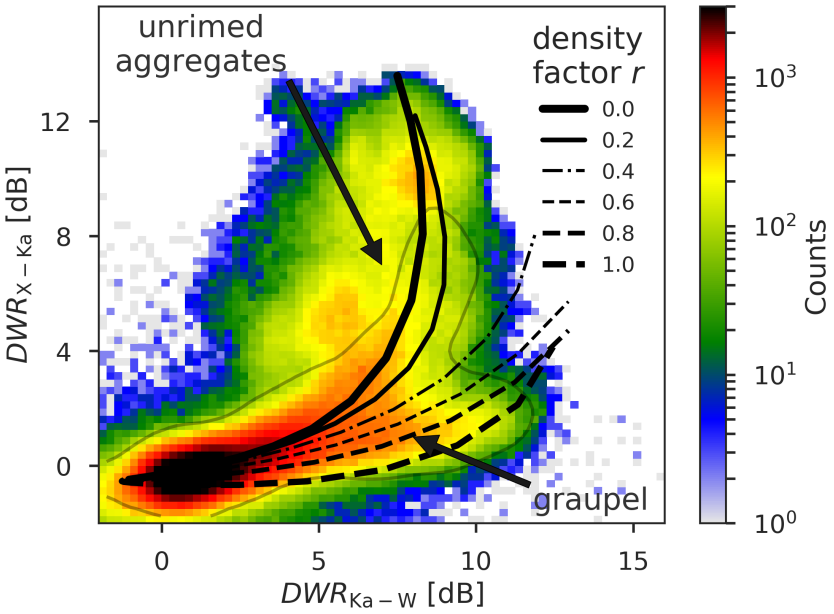

511 **Figure 5.** Joint histogram of measured dual-wavelength ratios (DWRs) for triple-frequency radar ob-
512 servations from the three cases studied in *Kneifel et al.* [2015]; a thin contour encloses the most frequent
513 measurements during the February 21–22 2014 case considered in Section 4.1, highlighting distinct features
514 associated with aggregates and graupel. Black curves represent the forward-modelled DWR for an expo-
515 nential distribution of particles with density factors from unrimed aggregates (using SSRGA for $r < 0.2$) to
516 graupel ("soft spheroids" for $r > 0.5$); the transition between rimed aggregates and graupel is represented by
517 an external mixture of the two approximations to the radar backscatter cross-section.

3 BAECC 2014 data

As part of the Biogenic Aerosols—Effects on Clouds and Climate field campaign [BAECC 2014; *Petäjä et al.*, 2016], the US Department of Energy atmospheric radiation measurement (ARM) program's second mobile facility (AMF2) was deployed at the University of Helsinki's Hyytiälä forestry field station (61°51'N, 24°17'E). The remote-sensing and in situ instrumentation, and their deployment are documented in *Kneifel et al.* [2015]. Between 1 February and 31 March 2014 the snowfall measurement experiment (SNEX) intensive observation period (IOP) focused on the measurement of snow microphysics. Remote-sensing observations include vertically-pointing Doppler radars, lidar and microwave radiometer instruments, and the state of the atmosphere from reanalysis (Section 3.1) will be evaluated against in situ measurements at the surface (Section 3.2).

3.1 Remote sensed measurements

Two vertically-pointing Doppler radars are the primary remote-sensing instruments in this study. The 35 GHz Ka-band Zenith Radar (KAZR) and the 95 GHz Marine W-band cloud radar (MWACR) were deployed at Hyytiälä during the SNEX IOP. Due to a mispointing of MWACR, mean Doppler velocity measurements from that radar are not used in this study. It is important that KAZR and MWACR sampling volumes are broadly overlapping; both radar measurements are resampled from approximately 2 s to 120 s. Calibration of MWACR and KAZR against a colocated vertically-pointing X-band radar is carried out as described in *Kneifel et al.* [2015], after accounting for attenuation due to atmospheric gases and liquid; when X-band radar is not available the most recent calibration is applied, and MWACR radar reflectivity is calibrated against KAZR radar reflectivity at cloud-top after correcting for attenuation.

Additional observations are available from the AMF2 high-spectral resolution lidar (HSRL), which measures molecular and particulate backscatter at 532 nm with gate spacing of 30 m and temporal resolution of 120 s. HSRL could be used for radar–lidar synergy retrievals of non-precipitating ice cloud, where the lidar provides valuable information on smaller ice particles and liquid droplets; however, in the rimed snow events of interest here the lidar is completely attenuated by liquid water near the surface. HSRL data are therefore presented alongside the radar data, but are not assimilated in the retrieval.

552 **Table 2.** AMF2 zenith-pointing radar instruments and observational uncertainties

Instrument	KAZR	MWACR
Frequency	35 GHz	95 GHz
Wavelength	8.6 mm	3.2 mm
Gate spacing	30 m	30 m
Beam width	0.38 °	0.3 °
Reflectivity uncertainty	1 dB	1 dB
Mean Doppler velocity uncertainty	0.5 m s^{-1}	n/a

560 Microwave radiometer (MWR) measurements at 23.8 and 31.4 GHz are used to re-
561 trieve liquid water path (LWP) and water vapour path [*Cadeddu et al.*, 2013]. While mi-
562 crowave radiometer measurements are not included in the retrieval, estimates of LWP pro-
563 vide information on the magnitude of supercooled liquid water (SLW) that are used to cor-
564 rect for radar attenuation due to liquid (discussed above and in Section 2.4) and to provide
565 context for the retrieval of riming based on the availability of supercooled liquid water in
566 mixed-phase clouds [e.g. *Kalesse et al.*, 2016; *Moisseev et al.*, 2017].

567 To assist in interpreting the remote-sensed data, atmospheric state profiles are obtained
568 from European Centre for Medium-Range Weather Forecasts (ECMWF) re-analysis at 1 hour
569 temporal resolution over the site. Variables are re-interpolated onto a height grid using pres-
570 sure measurements from 6 hourly radiosondes. Profiles of atmospheric temperature, pressure
571 and humidity are used in the target classification scheme and within the retrieval algorithm to
572 estimate radar attenuation due to atmospheric gases.

573 Prior to the retrieval remote-sensed and atmospheric data are averaged onto a com-
574 mon grid using the reflectivity-weighted mean Doppler velocity for averaging. A detection
575 mask is generated for each radar instrument, using the texture of the mean Doppler velocity
576 [*Helmus and Collis*, 2016] and radar signal-to-noise ratio after subtracting an estimate of the
577 noise.

578 ### 3.2 In situ measurements

579 The BAECC 2014 campaign provides a valuable opportunity to evaluate remote-sensed
580 estimates of snow against reliable and sustained in situ observations at the surface; this is

rarely possible at lower latitudes where both in situ and millimeter-wavelength radar measurements are affected by melting. Images of ice particles from the precipitation imaging package (PIP) video disdrometer [*Newman et al.*, 2009] are converted to measurements of particle number concentration, size, area and fallspeed. The mass of each particle is estimated from PIP observations of particle size, area and terminal velocity as described in *von Lerber et al.* [2017]; the maximum dimension of the ice particles are scaled to derive the particle masses that result in the best fit with snow accumulation measured by nearby Pluvio snow gauges. PIP measurements at 5 min resolution are used, and shifted by 5 minutes for comparison against remote-sensing measurements around 500 m above ground level. *Kneifel et al.* [2015] discuss a more precise approach to estimating the time-lag for evaluation against the lowest radar gates, but given the time-averaging used in this retrieval a constant lag was sufficient.

The median diameter D_0 and normalized number concentration N_w parameters are derived from the measured particle size distribution. Ice particle bulk density is estimated from PIP measurements using the measured PSD and velocity-size relation, and estimated mass-size relation according to (4) [*von Lerber et al.*, 2017]. This method was found to be consistent with complementary methods using the Pluvio snow accumulation to estimate the bulk density of ice [*Tiira et al.*, 2016; *Moisseev et al.*, 2017].

4 Results

We first demonstrate the retrieval for a case study (Sec. 4.1), before presenting statistical evaluation of retrievals over 10 snow events during the SNEX IOP (Sec. 4.2).

4.1 Case study: February 21–22 2014

At 23:00 UTC on February 21 2014 a warm occluded front passed over Hyytiälä, bringing about an hour of snow dominated by large aggregates. The light pre- and post-frontal snow was characterised by rimed particles, including both heavily rimed aggregates and graupel. With a total melted-equivalent accumulation of 5 mm comprising rimed and unrimed snow, this event has been extensively studied with in situ [*Tiira et al.*, 2016; *von Lerber et al.*, 2017; *Moisseev et al.*, 2017] and radar remote-sensing [*Kneifel et al.*, 2015; *Kalesse et al.*, 2016] methods. The remote-sensed and in situ measurements for this case are

shown in Figs. 6 and 7, respectively. We divide the case into pre-frontal, frontal and post-frontal regimes.

In the prefrontal regime (18:00 to 23:00 UTC) snowfall is relatively constant with melted-equivalent rates between 0.2 and 1 mm h^{-1} (Fig. 7d) from clouds with tops around 5 km and −20 °C (Fig. 6a–c). Particles measured in situ are dominated by a high concentration of compact ice particles, with bulk densities between 200–400 kg m^{-3}. PIP imagery confirms the presence of graupel during this period [Fig. 14 from *Kneifel et al.*, 2015]. In the hour prior to the front, cloud-top lowers to around 3 km and −15 °C, and relatively little snow is measured at the surface. *Moisseev et al.* [2017] and *von Lerber et al.* [2017] note that the low particle counts measured by PIP during this period lead to reduced confidence in the retrieved quantities, and the bulk density (Fig. 7d) is not retrieved here.

The frontal regime (23:00 and 00:00 UTC) brings heavier snow with a peak snowfall rate of 4.0 mm h^{-1}, and PIP imagery and measurements indicate large aggregates with median diameters up to 5 mm (Fig. 7d); however, particle fallspeeds do not exceed 1.5 m s^{-1} (Fig. 7b). Here cloud-top is around 9 km and the maximum KAZR reflectivity factor exceeds 20 dBZ near the surface.

The post-frontal regime (00:00 to 03:00 UTC) is dominated by patchy and very light snow with the exception of two showers in which the snow rate exceeds 2 mm h^{-1}; cloud-top is again between 3 and 5 km. PIP measurements of bulk density are higher than in the pre-frontal period, between 200 and 500 kg m^{-3}, and the particle size distribution confirms that the post-frontal snow features a higher concentration of larger and fast-falling particles, which *von Lerber et al.* [2017] noted comprised a mixture of rimed aggregates and graupel.

The presence of rimed snow and graupel throughout the pre- and post-frontal regimes is indicative of persistent mixed-phase cloud layers in the lower atmosphere; however, the vertical distribution of supercooled liquid water cannot be observed directly. The liquid water path retrieved from microwave radiometer (Fig. 6f) and strong HSRL backscatter (Fig. 6d) in the lowest liquid layers suggest that the vertically-integrated amount of liquid water increases throughout the case, while the cloud base lowers. Above this lowest layer, *Kalesse et al.* [2016] used Doppler spectra and soundings to infer the presence of embedded mixed-phase cloud layers around 1 and 3.2 km. The exception is in the frontal snow, when both microwave radiometer and lidar backscatter indicate that the liquid water layers are depleted [*Moisseev et al.*, 2017]. Visual inspection of the mean Doppler velocity (Fig. 6c) hints at the

signature of mixed-phase cloud layers in the reflectivity-weighted average fallspeed of snow particles: the largest near-surface mean Doppler velocities correspond in time to maxima in LWP around 22:00, 01:00 and 02:20 UTC (Fig. 6f) during the pre- and post-frontal regimes, while the frontal regime represents a minimum in both mean Doppler velocity and LWP despite being the period during which the greatest snow rate and particle size are measured. Through the vertical profile, increases in the mean Doppler velocity are evident at or around 1 and 3 km, which may be related to the onset of riming in mixed-phase cloud layers. A more quantitative estimate of riming will be made using the CAPTIVATE retrieval algorithm.

The CAPTIVATE retrieval is applied to the February 21 case, assimilating 35- and 94-GHz radar reflectivities and 35-GHZ mean Doppler velocity (hereafter "ZZV"). Recall that the 94-GHz Doppler velocity is not used due to a mispointing error. The retrieved state variables are the extinction coefficient, primed number concentration and density index (hereafter "$\alpha_v N_0' r'$"). As a check on the quality of the retrieval, we confirm that the best estimate of the state can be used to forward-model the observed MWACR radar reflectivity (Fig. 8a&b) and KAZR mean Doppler velocity (Fig. 8c&d). Rather than report the values of the state variables directly, we derive more physically meaningful parameters from the retrieval: the melted-equivalent snow rate (Fig. 8e), normalized number concentration (Fig. 8f), median diameter (Fig. 8g), and the density factor (Fig. 8h). In the prefrontal regime snow rate reaches 0.1–1.0 mm h^{-1} below 3 km. In the frontal regime the snow rate exceeds 1 mm h^{-1} between 5–7 km above ground level; toward the surface, number concentration decreases while median diameter increases, suggesting growth by aggregation. In the post-frontal showers maxima in snow rate correspond to streaks of increased number concentration and median diameter. Of primary interest is the retrieval of the density factor, which increases to around $r = 0.2$ below 3 km in the pre-frontal and post-frontal regimes and up to local maxima of 0.5 to 0.7 near the surface around 22:00, 01:00 and 02:20 UTC; in short, the retrieved density factor maps closely to the regions of high mean Doppler velocity identified earlier. In the pre-frontal regime small but non-zero density factors are retrieved in both the cirrus and the midlevel cloud-tops, albeit with large estimated uncertainties (not shown); much of this cirrus occurs below temperatures at which supercooled liquid—and therefore riming—is to be expected (Fig. 6a–c), an occurrence which has not been excluded within the retrieval. As discussed in Section 2.2.2, small non-zero density factors are within the observed variability of mass-size relations for unrimed particles; however it may also be the case that vertical air motion dominates the mean Doppler velocity in this regions.

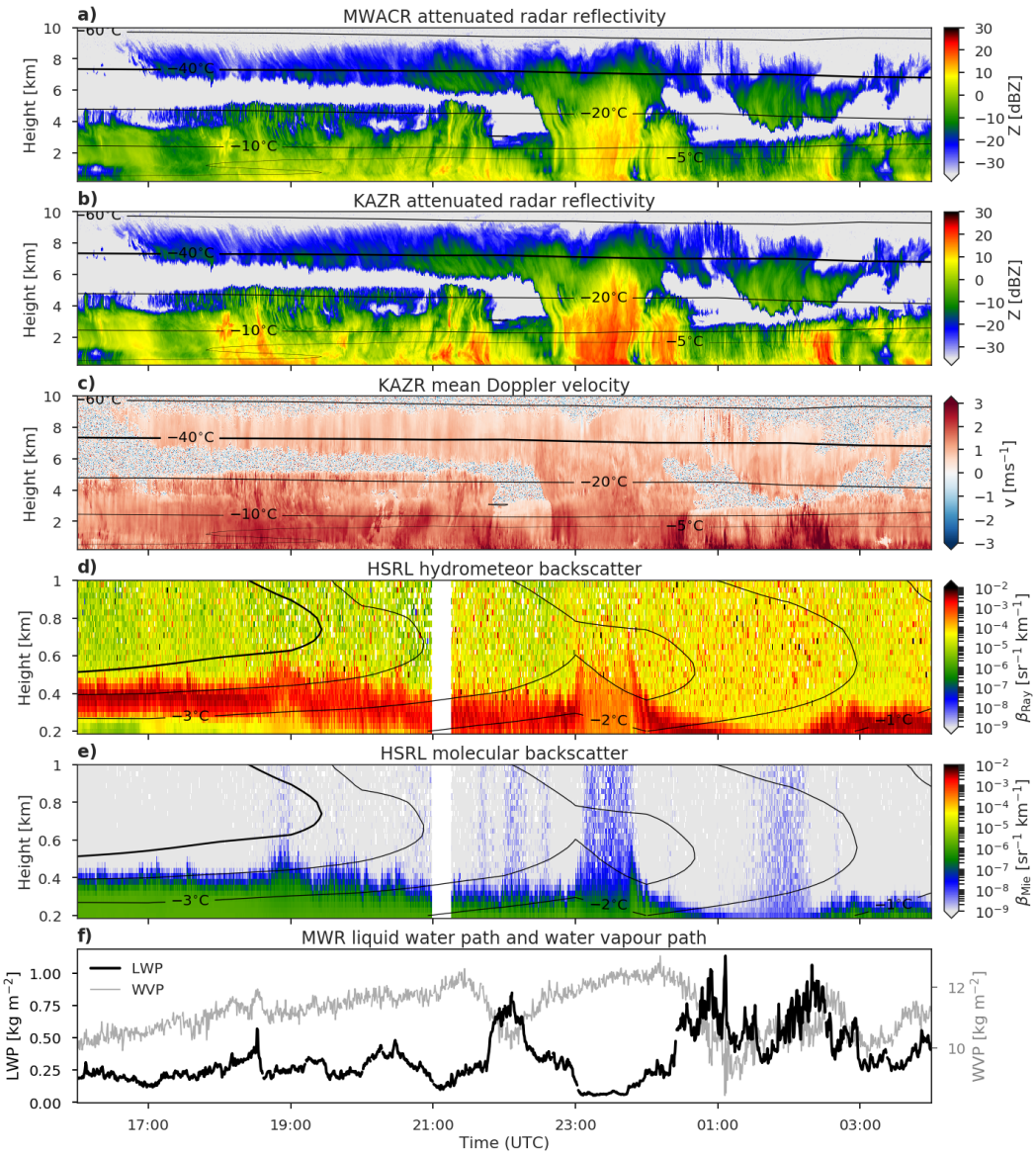

Figure 6. AMF2 measurements from Hyytiälä between 2014-02-21 16:00 UTC and 2014-02-22 03:00 UTC. KAZR radar reflectivity (a) and mean Doppler velocity (b); MWACR radar reflectivity (c); HSRL attenuated Mie backscatter (d) and attenuated Rayleigh backscatter (e); and microwave radiometer LWP (f). Note the different vertical scales for HSRL backscatter (d & e). Black contours are temperature from ECMWF re-analysis; a darker line at −40°C denotes the temperature below which supercooled liquid water is not expected.

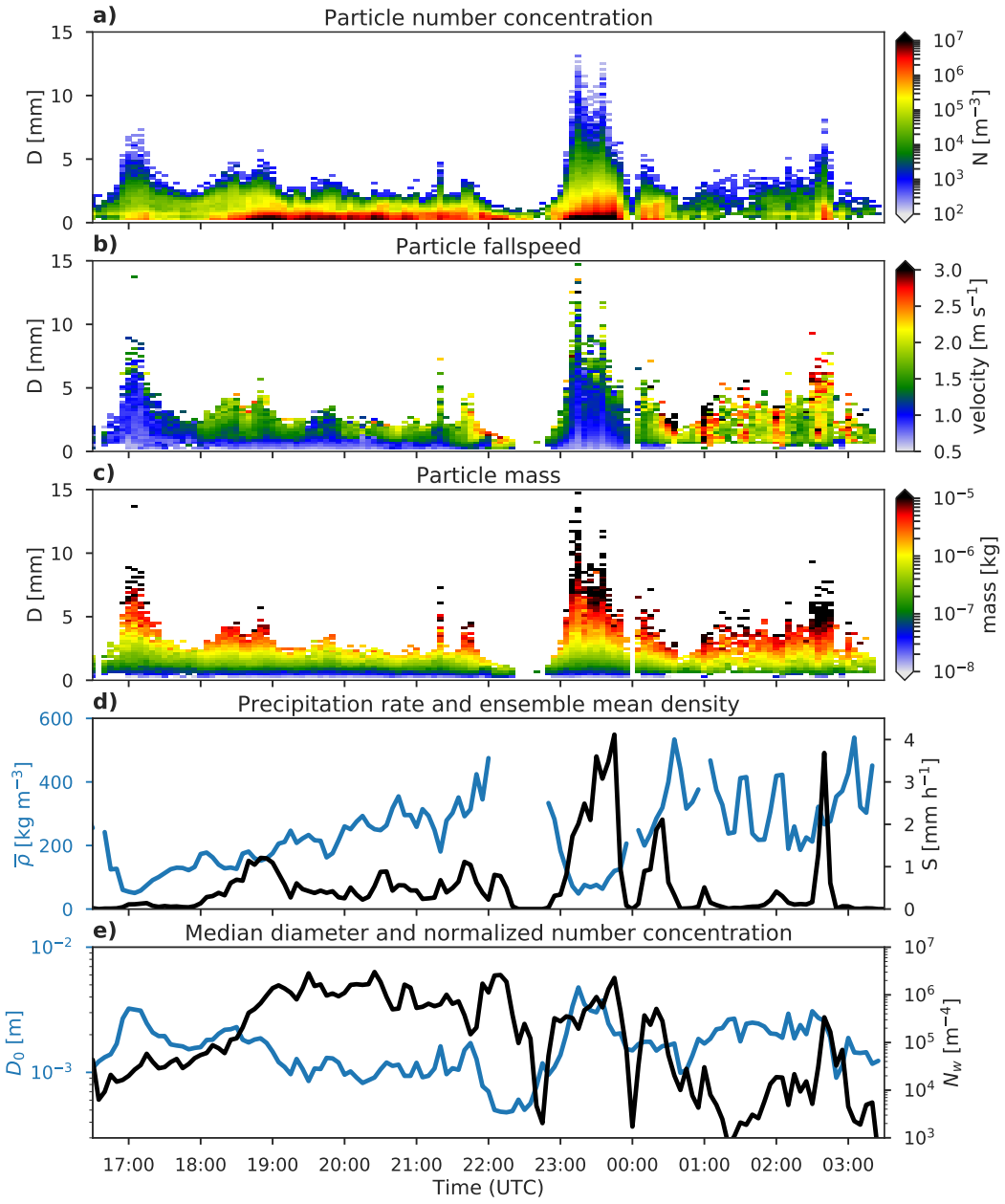

656 **Figure 7.** In situ PIP measurements from Hyytiälä between 2014-02-21 16:00 UTC and 2014-02-22 05:00
657 UTC. Particle size and fallspeed are measured, while particle mass, snow rate and bulk density are estimated
658 as described in *von Lerber et al.* [2017].

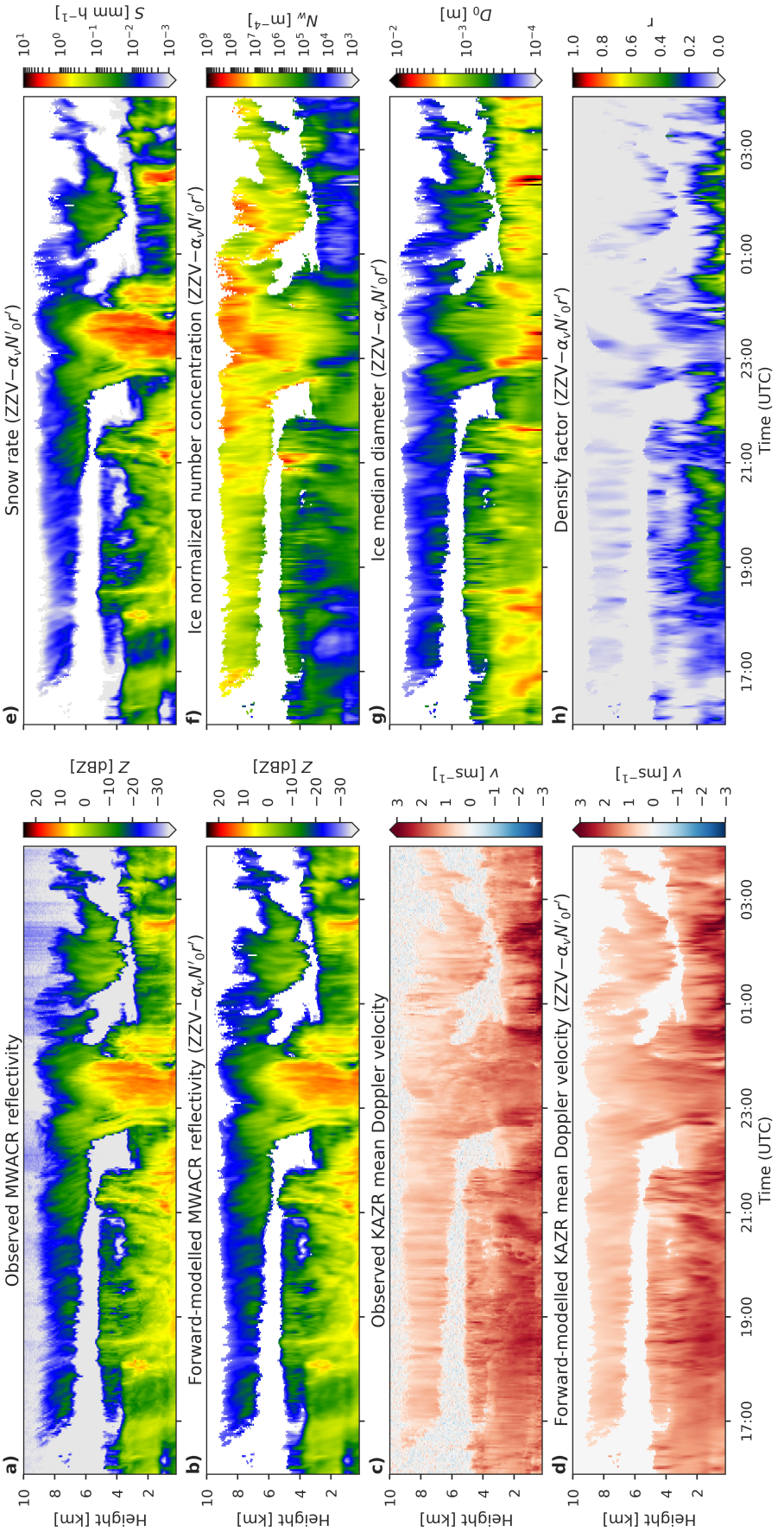

Figure 8. The observed and forward-modelled MWACR reflectivity (a & b), and observed and forward-modelled KAZR mean Doppler velocity (c & d); and the retrieved snow rate (e), normalized number concentration (f), median particle diameter (g) and density factor (h) from the ZZV retrieval for the 21 February 2014 case.

4.1.1 Profiles

In addition to assimilating all available radar measurements and retrieving all state variables, it is of interest to explore the relative contributions of Doppler and dual-frequency measurements to the CAPTIVATE retrieval. These configurations are more easily compared at selected profiles, each representing 120 S of averaged radar measurements. We select a profile from each of the snow regimes: a pre-frontal profile at 21:30 UTC (Fig. 9 I), a frontal profile at 23:20 UTC (Fig. 9 II), and a post-frontal profile at 02:20 UTC (Fig. 9 III).

The ZZV–$\alpha_v N_0' r'$ retrieval of the pre-frontal profile (Fig. 9 I) shows snow rate increasing below 3 km to approximately 0.5 mm h^{-1} at the surface, concurrent with an increase in the density factor to around $r = 0.3$ below 1 km. Large uncertainties in the retrieved density factor reflect a large observational uncertainty of 1 m s^{-1} in the Doppler velocity; however, we find that the retrieved density factor is robust to changes in the observational uncertainty. When Doppler velocity is not assimilated (ZZ–$\alpha_v N_0' r'$) there is little constraint on the density factor, which remains close to $r = 0$. This leads to an underestimate in forward-modelled mean Doppler velocity of as much as 1 m s^{-1} below 2 km, and N_w greater by a factor of 5 than that of ZZV–$\alpha_v N_0' r'$; that is, when dense rimed particles are not retrieved, the lower density of ice is compensated by a larger concentration of snow particles such that the snow rate differs only slightly from that of ZZV–$\alpha_v N_0' r'$. The ZZ–$\alpha_v N_0' r'$ retrieval is very similar to one in which Doppler velocity is available, but where all snow is assumed to be unrimed aggregates (ZZV$-\alpha_v N_0'$; not shown). Conversely, when only MWACR reflectivities are assimilated and the full state vector is retrieved (Z94V–$\alpha_v N_0' r'$; the dark green line in Fig. 9 I), the PSD diverges significantly from ZZV–$\alpha_v N_0' r'$. A much lower number concentration of larger particles is retrieved, with median diameter a factor of two larger than that of ZZV–$\alpha_v N_0' r'$. Despite a lower density factor, this retrieval appears well-constrained by the Doppler velocity—but the forward-modelled DWR indicates that the larger particles lead to an error in Ka-band reflectivity of around 4 dB near the surface. This is an example of an under-constrained retrieval in which three state variables are estimated from two measured variables. A better-posed retrieval can be made by treating the primed number concentration as a model variable which does not vary from the prior Z94V–$\alpha_v r'$ (the bright green line in Fig. 9). The results of this retrieval much more closely resemble ZZV–$\alpha_v N_0' r'$, with reduced errors in forward-modelled DWR and values of N_0' and D_0 closer to their priors; therefore in subsequent profiles only the Z94V–$\alpha_v r'$ will be compared with ZZV–$\alpha_v N_0' r'$ and ZZ–$\alpha_v N_0' r'$.

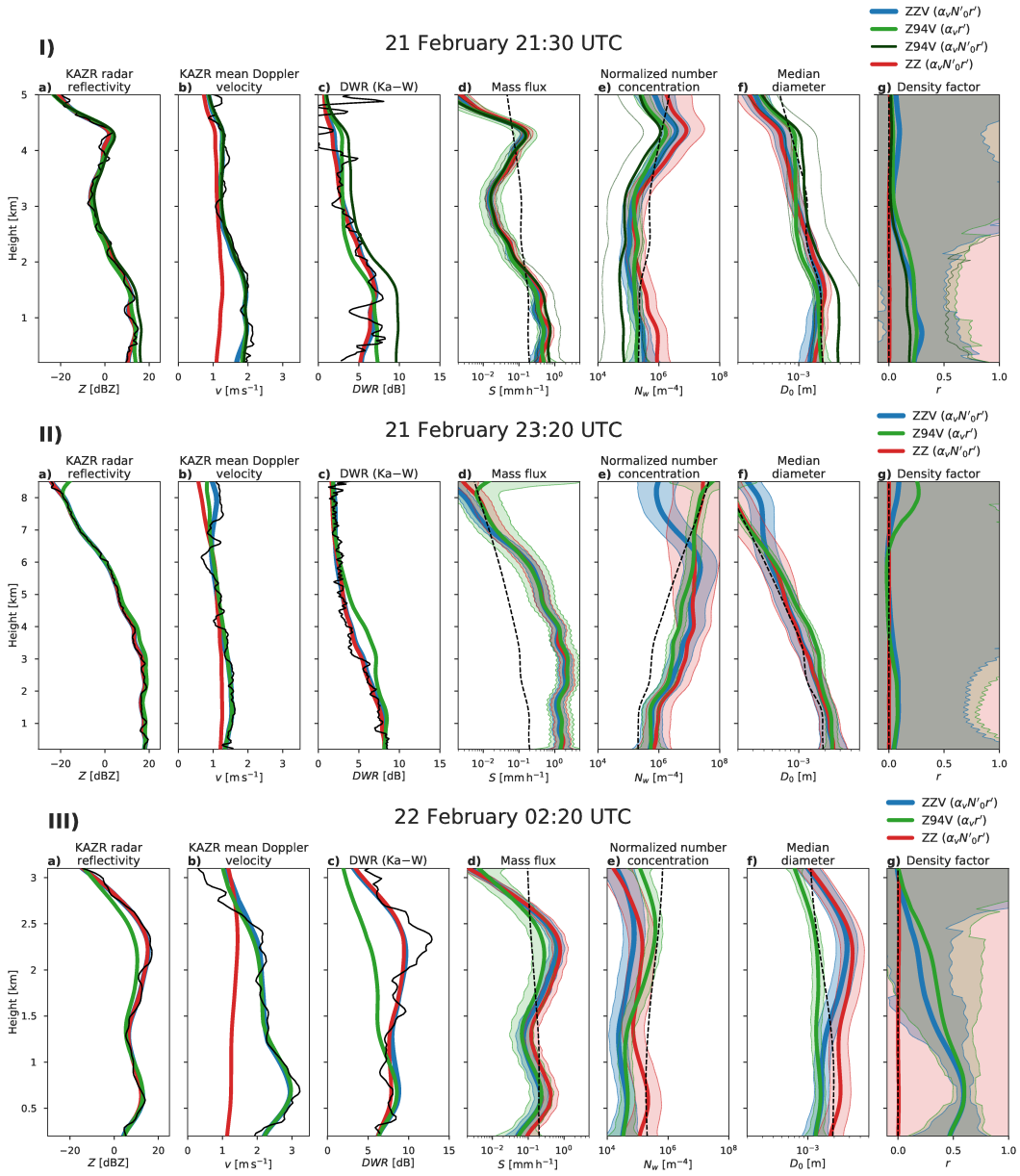

691 **Figure 9.** Forward-modelled measured variables and retrieved snow rate, normalized number concentra-
692 tion, median diameter and density factor for ZZV, Z94V and ZZ retrievals, for a profile at 21:30 UTC (I) ,
693 23:20 UTC (II) and 02:20 UTC (III) within the pre-frontal regime. Black solid lines indicate the observed
694 variables, and dashed lines indicate the prior retrieved variables. Shading indicates the 5th to 95th percentile
695 uncertainty of the retrieval.

In the frontal regime (Fig. 9 II) there is generally good agreement between retrievals, which consistently represent a snow rate of 1 to 2 mm h^{-1} below 4 km; this relatively constant mass flux corresponds with increasing median diameter and decreasing number concentration consistent with strong aggregation in the shower, and confirmed by the large aggregate snowflakes observed at the surface (Fig. 7). Both ZZV and Z94V diagnose smallnon-zero density factors below about 4 km, without which ZZ under-estimates the mean Doppler velocity by around 0.5 m s^{-1}. In the mid-levels Z94V overestimates KAZR radar reflectivities, once again due to a smaller concentration of larger particles. In most other regards the retrievals are similar until near cloud-top, where relatively large Doppler velocities lead to the retrieval of small to moderate density factors in ZZV and Z94V which are unphysical (the contours in Fig. 6 indicate that the temperature is below −40°C at these heights), and may be a result of vertical air motion in the cirrus. In stratiform precipitation, the retrieval of dense ice due to small-scale turbulent features in vertical air motion is somewhat suppressed by the use of a Kalman smoother in the retrieval of the density index; however, it would also be possible within CAPTIVATE to reduce prior uncertainty in the density factor where riming is unlikely, or to apply higher uncertainties to mean Doppler velocity measurements where larger contributions from vertical air motion are expected.

In the postfrontal regime (Fig. 9 III) the Doppler velocity reaches 3 m s^{-1} below 1 km, where ZZV and Z94V estimate density factors around $r = 0.6$; ZZ does not diagnose resolve this increase in particle density, and the corresponding forward-modelled mean Doppler velocity differs from observations by almost 2 m s^{-1} along with overestimates in both number concentration and median size. While ZZV and Z94V converge upon similar PSDs below 1.5 km where the Doppler signal is strong, near the top of the cloud Z94V remains closer to its priors (recall that N_0' does not vary in this retrieval), leading to a much higher concentration of small particles and a significant under-estimate of the KAZR radar reflectivity above 1.5 km.

While the uncertainties in the retrieved density factor are constrained in the parts of the profile where the mean Doppler velocity of denser particles differ significantly from that of unrimed aggregates—typically below 2 or 3 km in these profiles—very large density factor uncertainties are evident aloft. In these regions the Doppler velocity contains little information about variations in density because the smallest particles are assumed to be solid quasi-spheroidal particles for all values of the density factor (see Fig. 3).

754 ### *4.1.2 Comparison against in situ measurements*

755 We now evaluate the CAPTIVATE retrievals against in situ measurements at the sur-
756 face; ZZV, Z94V and ZZ estimates of snow rate, normalized number concentration, median
757 diameter, and bulk density averaged over the radar gates up to 600 m above ground level are
758 compared against those from PIP (Fig. 10).

759 All of the CAPTIVATE retrievals of snow rate are within the range of uncertainty of
760 PIP snow rate, with under-estimates of up to 50 % especially evident in frontal and post-
761 frontal showers. As was also the case in the analysis of profiles, the estimated snow rates are
762 remarkably consistent between the different retrievals; this is despite significant differences
763 in estimates of particle size, number concentration and density.

769 As they often compensate for one another, the parameters of the PSD are evaluated
770 together. ZZV and ZZ estimates of median diameter (Fig 10c) are within 50 % of PIP mea-
771 surements, and estimates of normalized number concentration (Fig 10b) are usually within
772 the retrieval uncertainty—with errors of up to a factor of five—of PIP measurements. With-
773 out a dual-frequency constraint on particle size and therefore fewer state variables retrieved,
774 the Z94V$-\alpha_v r'$ estimates of N_0' and D_0 are less able to resolve the distinct snow regimes: in
775 the pre-frontal period Z94V number concentrations exceed PIP measurements by up to an or-
776 der of magnitude while particle sizes may be double the surface observations; the inverse is
777 true in the post-frontal period.

778 Finally we evaluate the retrieval against in situ measurements of bulk density (Fig. 10d).
779 The volume flux-weighted bulk density is estimated from retrieved particle properties consis-
780 tent with eq. 4, in which the mass- and velocity-size relations are modulated by the retrieved
781 density factor. We compare this remote-sensed estimate against two in situ retrievals of bulk
782 density from PIP measurements [*von Lerber et al.*, 2017] and a combination of PIP and Plu-
783 vio snow gauge measurements [*Moisseev et al.*, 2017] to constrain the total accumulation; we
784 note that the former method was calibrated against the latter, so these two retrievals are not
785 independent. The retrieved density factor and median diameter are both important to the es-
786 timated bulk density; when constrained by both Doppler and dual-frequency measurements,
787 ZZV is therefore broadly capable of resolving the bulk density measured by PIP, although
788 we note underestimates of 25–50 % between 20:30 and 22:00 in the pre-frontal period, and
789 between 01:00 and 01:45 in the post-frontal period. Errors in Z94V estimates of median di-
790 ameter can either exacerbate (in the pre-frontal regime) or mask (in the post-frontal) errors

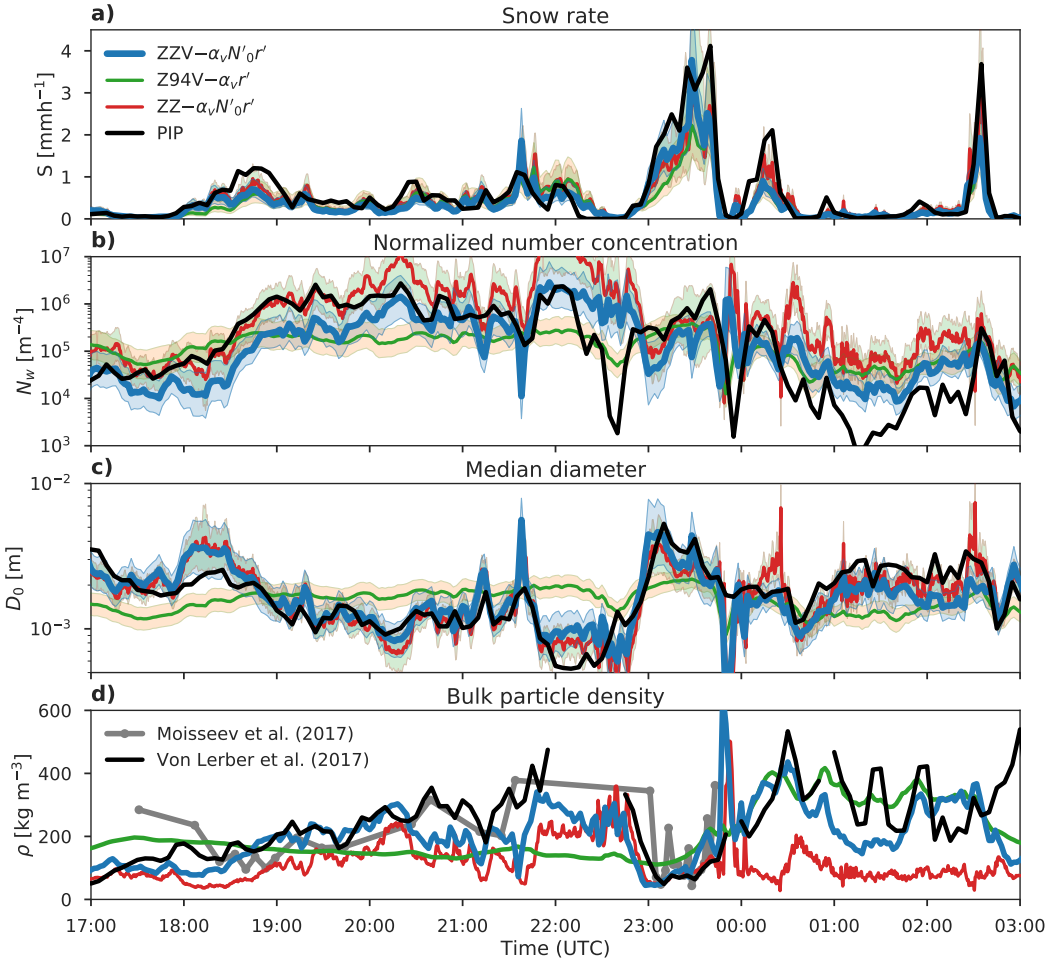

Figure 10. Time series comparing mean retrieved variables over the lowest radar gates (between 300 m and 600 m) against the in situ PIP measurements at the surface. Shaded areas indicate the 5th and 95th percentile uncertainty of the retrieval. Surface observations are shifted by 5 minutes. The bulk ice density is discontinuous where very small median diameter leads to erroneously high densities, as discussed in *von Lerber et al.* [2017].

in the bulk density: as discussed above, with a weaker constraint on particle size Z94V does not resolve the compact graupel ahead of the front, and underestimates post-frontal particle size. Conversely, without Doppler information the bulk density estimates from ZZ are chiefly a function of particle size: density rarely exceeds 200 kg m^{-3} except immediately ahead of the front, when median diameters of less than 1 mm are estimated.

4.1.3 Riming as an indicator of mixed-phase cloud

While CAPTIVATE has been developed for radar–lidar–radiometer synergy retrievals, in the present case the lidar is fully extinguished within less than 1 km of the surface in the lowest of several shallow layers of mixed-phase cloud. Our retrievals assimilate radar reflectivity and mean Doppler velocity, both of which are dominated by backscatter from larger ice particles; the Doppler spectrum or its higher moments can sometimes be used to identify the presence of liquid cloud [*Kalesse et al.*, 2016], although the broader applicability of these methods can be limited, especially for retrievals from airborne and spaceborne platforms where spectral broadening is significant [e.g. *Illingworth et al.*, 2015]. The density of ice particles has been retrieved based on mean Doppler velocity, relying on approximations to the morphology of ice particles from unrimed aggregates to graupel and their associated terminal fallspeeds. We hypothesise that the primary process by which high density factors occur is the riming of ice particles within mixed-phase clouds. An independent source of information on the potential for riming is LWP retrieved from the microwave radiometer; *von Lerber et al.* [2017] used LWP as a proxy for riming, and the connection between LWP and rime mass fraction is also demonstrated from in situ retrievals in *Moisseev et al.* [2017].

For the present case, the timeseries of LWP is strongly correlated to the CAPTIVATE retrievals of density factor in the near-surface gates (Fig. 11a; ZZV-$\alpha_v N_0' r'$). The highest density factors correspond to the presence of significant mixed-phase cloud in the pre- and post-frontal periods, and the dominance of unrimed aggregates to the depletion of liquid evident during the frontal snow. The scatter plot of the LWP versus the retrieved density factor (Fig. 11b) is coloured by the mean Doppler velocity and sized by retrieved median diameter. At low LWP particles tend to be large unrimed aggregates with mean Doppler velocities less than 2 m s^{-1}. Moderate LWP profiles correspond to particles ranging from larger rimed aggregates with $0.0 < r < 0.2$, to compact rimed aggregates ($0.2 < r < 0.5$). At high LWP the snow is dominated by graupel ($0.5 < r < 0.8$), with some instances of larger, fast-falling and heavily-rimed aggregates.

In summary, the February 21 2014 case study includes significant riming below around 3 km during pre- and post-frontal snow, interrupted by a frontal shower dominated by large aggregate snowflakes. Mean Doppler velocity provides an effective constraint on estimates of the density factor, retrieved values of which varied from $r \approx 0.1$ for unrimed aggregates $r \approx 0.6$ for graupel. Dual-frequency radar reflectivity proved critical to constraining estimates of the particle size distribution, leading to significant improvements in retrieved quantities when compared with in situ measurements at the surface. While the single-frequency retrieval was capable of similar estimates of snow rate and density factor, the retrieval was better constrained when a single parameter of the PSD was retrieved, leading to estimates closer to the priors in which compact pre-frontal graupel was not resolved. Our hypothesis that the retrieved density factor varies chiefly due to the riming of ice particles in mixed-phase cloud layers is supported by a strong association between the density factor and an independent estimate of supercooled liquid water.

4.2 SNEX 2014 IOP

In this section the LWP is used as an indicator of the availability of SLW for riming, hence to distinguish between unrimed and rimed snow, and heavily rimed snow or graupel. Snow events during the SNEX IOP were identified by *von Lerber et al.* [2017] wherein significant snow was falling at the surface and the surface temperature was below freezing (Table 3). A probability density function of LWP over the SNEX IOP (Fig. 12a) illustrates that, while the majority of the snow events during the period occurred in low-LWP conditions, significant SLW is relatively frequent during the IOP. Following a similar distinction made in *von Lerber et al.* [2017], three ranges of LWP are used to distinguish between unrimed (LWP $< 0.1\,\mathrm{kg\,m^{-2}}$), moderately rimed ($0.1 \leq$ LWP $< 0.3\,\mathrm{kg\,m^{-2}}$), and heavily rimed snow or graupel (LWP $\geq 0.3\,\mathrm{kg\,m^{-2}}$). In that study the mass-size and fallspeed-size relations from in situ measurements of particles were shown to be consistent with the LWP classification. Unrimed snow accounts for just over half of the profiles; rimed snow around 30 %, and graupel around 10 %; in the rest, no significant snow was measured and the profile was skipped. While the unrimed snow is associated with the coldest surface temperatures (Fig. 12b) on average, all three categories are most frequent at temperatures just below freezing; it is not evident that the riming events can be distinguished by temperature. Similarly, the low-LWP regime includes almost all events with low relative humidities (Fig. 12c), but all categories occur most frequently at relative humidities greater than around 90 %.

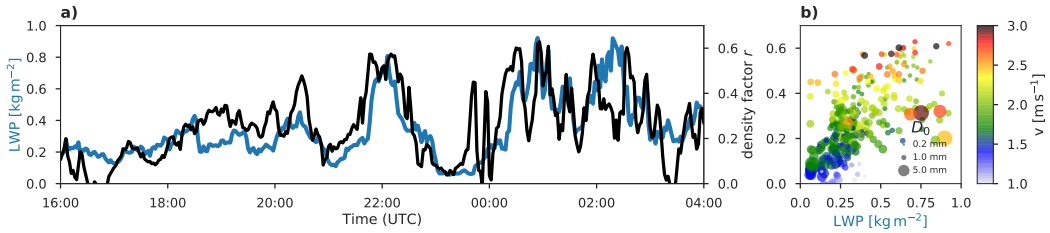

Figure 11. Time series (a) and scatter plot (b) of ZZV$-\alpha_v N_0' r'$ density factor in the lowest radar gates (300m to 600m) against LWP measured by the microwave radiometer. In the scatter plot the markers are coloured by the mean Doppler velocity, and sized according to the retrieved median diameter.

Table 3. Snow events during SNEX 2014 IOP

Date (UTC) 2014	Melted-equivalent accumulation [mm]	Surface temperature (°C) Min	Max
*1 Feb 00:00—06:00	7.4	−9.8	−8.9
*1 Feb 10:00—16:00	1.4	−7.9	−7.0
2 Feb 16:00—19:00	1.7	−5.4	−5.2
12 Feb 04:00—09:00	0.8	−1.0	0.0
15 Feb 21:00—16 Feb 02:00	2.6	−2.1	−1.0
21 Feb 16:00—22 Feb 03:30	5.0	−2.7	0.0
15 Mar 05:00—07:00	0.3	−2.0	−1.3
*18 Mar 08:00—19:00	4.4	−3.8	−1.8
19 Mar 00:00—20:00	1.5	−7.3	−3.7
20 Mar 16:00—00:00	6.1	−4.3	−1.3

* Denotes events where dual-frequency radar data were not always available.

The CAPTIVATE best estimate (ZZV$-\alpha_v N_0' r'$) was run over approximately 55 hours of available dual-frequency Doppler radar data. Joint histograms of the profile of forward-modelled observed variables and retrieved variables are shown for each of the LWP classifications (Fig. 13).

The unrimed snow (Fig. 13-I; $LWP < 0.1\,\mathrm{kg\,m^{-3}}$) is associated with the lowest mean Doppler velocities (Fig. 13-Ib), which average around $1\,\mathrm{m\,s^{-1}}$ near the surface and never exceed $2\,\mathrm{m\,s^{-1}}$. The corresponding median density factor (Fig. 13-Ig) is between 0 and 0.2 below 4 km; this is consistent with the finding of *Moisseev et al.* [2017] that the mass-size of unrimed aggregate snow at Hyytiälä is consistently higher than that of *Brown and Francis* [1995], corresponding to roughly $r = 0.15$ in Fig. 1. In the earlier profile of unrimed snow (Fig. 9 II) it was noted that ice water content remained constant with height near the surface while diameter increased and number concentration decreased; these characteristic features of aggregation are robustly present in approximately 30 hours of aggregate snowfall, with the median snow rate (Fig. 13-Id) constant below 3 km, concurrent with an increase in median size (Fig. 13-If) and a decrease in number concentration (Fig. 13-Ie) toward the surface. The gradient in D_0 represents roughly a doubling in median particle diameter over 2 km. The Ka-W dual-wavelength ratio increases below 3 or 4 km to a median of around 5 dB; however, comparison to the triple-frequency data (Fig. 5) shows that values in this range are not unique to either aggregates or graupel; a third radar frequency would provide valuable information to help constrain a retrieval based on the different scattering signatures of unrimed aggregates and heavily rimed particles.

In the rimed snow (Fig. 13 II; $0.1 \leq LWP < 0.3\,\mathrm{kg\,m^{-3}}$) mean Doppler velocities (Fig. 13IIb) are between 1 and $2\,\mathrm{m\,s^{-1}}$ near the surface, corresponding to density factors that increase below about 4 km to between 0 and 0.4 in the lowest 2 km. Unlike the unrimed snow, the snow rate (Fig. 13 IId) continues to increase toward the surface, indicating an addition of ice water content which may be due to accretion of supercooled liquid or vapour deposition. The near-surface gradients of N_0' and D_0 (Fig. 13 IIe & f) are not significantly reduced from those in unrimed snow, so it seems likely that a mix of aggregation, riming and deposition processes occur within this regime.

Finally, the heavily rimed snow or graupel (Fig. 13 III; $LWP \geq 0.3\,\mathrm{kg\,m^{-3}}$) is associated with mean Doppler velocities (Fig. 13 IIIb) up to $3\,\mathrm{m\,s^{-1}}$ and density factors (Fig. 13 IIIg) increasing steeply below 3 km up to as much as $r = 0.5$ with a median around $r = 0.3$.

Unlike the unrimed and rimed snow regimes, the snow rate in this regime increases rapidly toward the surface, with the median snow rate increasing by an order of magnitude over the lowest 2 to 3 km—a rate similar to that in the upper-level clouds of all regimes—however, D_0 and N_0' are near-constant in the lower levels. This is consistent with an accretion of mass due to riming, although deposition cannot be ruled out. An increase in normalized number concentration may be discernible near the surface (Fig. 13 IIIg), perhaps suggesting a relative increase in the concentration of small particles, or a breakup of larger particles. This may be indicative of a secondary ice generation process such as rime splintering; however, more work would be required to confirm this, and to what degree the present retrieval may help in the study of secondary ice processes.

An evaluation of the CAPTIVATE retrieval over all available dual-frequency Doppler radar data from the SNEX IOP has shown characteristic differences between the profiles of snow rate, PSD parameters and density factor between profiles of unrimed and rimed snow. LWP provides a suitable proxy to distinguish between unrimed and heavily rimed snow events. This initial analysis has focused on demonstrating the potential to resolve key microphysical processes from the Doppler velocity; however, many other analyses of the meteorological and thermodynamical context of riming and aggregation processes may be envisaged.

5 Discussion and conclusions

The morphology of an ice particle is a record of the microphysical processes by which it forms; in this study we have proposed a simple parameterisation for the representation of the wide range of ice particle densities and shapes from unrimed aggregate snowflakes to graupel and hail. Remote-sensed estimates of snow typically assume snow particles that resemble unrimed aggregates; however, riming is both a critical process for surface hydrology and a control on radiatively-important mixed-phase clouds which are difficult to remote-sense and poorly represented in numerical models. We have demonstrated a method for diagnosing riming within the framework of CAPTIVATE, an optimal estimation algorithm for radar–lidar–radiometer retrievals of clouds, aerosols and precipitation.

The retrieved density factor modulates the density, shape and radar scattering cross-section of ice particles, and is chiefly inferred from mean Doppler velocity, a measure of reflectivity-weighted particle terminal velocities. Many refinements to this parameterisation may be envisaged to better represent the microphysical processes in question, and the

sensitivity of the retrieval to the formulation of the density factor and its effect on the mass, area and scattering cross-sections of ice particles requires further study. An alternative parameterisation intended to more closely resemble the conceptual model for the riming of aggregate snowflakes was tested using a reference mass-size relation for unrimed aggregates at Hyytiälä [*von Lerber et al.*, 2017] with a constant exponent of $b_m = 2.1$, and where only the prefactor of the mass-size relation was scaled with the density factor. This representation is more consistent with the conceptual model of the "in-filling" stage of riming, but does not encompass the observed variability amongst unrimed snowflakes or the higher exponents of heavily rimed graupel-like particles. The retrieved snow rate and PSD were not strongly sensitive to changes in how particle density is allowed to vary, suggesting the two parameterisations allow for similar representation of unrimed to lightly rimed aggregates despite some change in the mass-size exponent; however, in situ measurements of snow rate and bulk particle density agreed better with the original retrieval in the densest post-frontal snow, suggesting the advantages of representing a broader range of particle morphologies, especially of heavily rimed graupel-like particles. Our prior density factor of $r = 0$ relates to the unrimed aggregates of *Brown and Francis* [1995], but it may be possible to implement more sophisticated priors or constraints on the retrieval based on the atmospheric state [e.g. *Lin and Colle*, 2011; *Szyrmer and Zawadzki*, 2014], or from regional climatologies, to better resolve this variability; for example, *Moisseev et al.* [2017] showed that the lowest-density particles at Hyytiälä were significantly more dense than those of *Brown and Francis* [1995], and this could be represented with an updated prior of $r \approx 0.15$ near the surface. Concurrent remote-sensed and in situ measurements from the BAECC 2014 campaign have provided an invaluable opportunity to evaluate retrievals of rimed snow. Sustained particle imaging and multiple-frequency radar measurements from Hyytiälä and other ARM and CloudNet "supersites" will provide critical datasets for the improved representation of snow microphysics, as well as validation for future satellite retrievals.

The CAPTIVATE retrieval was applied to vertically-pointing Ka- and W-band Doppler radar measurements from 10 snow events over the SNEX IOP of BAECC 2014. Dual-frequency and Doppler radar measurements provided sufficient information to retrieve two parameters of the PSD as well as the density factor. The dual-frequency radar reflectivities and mean Doppler velocity make distinct contributions to the retrieval, with radar reflectivities at Ka- and W bands providing a strong constraint on the particle size distribution but relatively little information on density; Doppler velocity provided the sole constraint on the density factor.

Estimates of near-surface snow rate were within 50 % of in situ measurements both with and without Doppler and dual-frequency measurements, showing a remarkably robust retrieval of ice water content from 94-GHz radar reflectivity; however, to accurately estimate the parameters of the PSD as well as the bulk ice density, it was important to have both dual-frequency and Doppler information. With the recent availability of multiple-frequency Doppler radar observations of snow, and supported by observational and theoretical insights into the triple-frequency signatures of rimed and unrimed ice [e.g. *Kneifel et al.*, 2018], it will become increasingly important to quantify the information content of each additional observational variable within an optimal estimation framework.

The retrieval of riming provides an indirect insight into the presence of supercooled liquid water, and it may hence be possible to use spaceborne Doppler radars to better quantify the frequency and distribution of embedded mixed-phase clouds—at least where precipitating ice is present. Using LWP as a proxy for riming provided a robust distinction between retrieved snow profiles of unrimed aggregates, rimed aggregates and graupel; no such clear distinction was evident in surface temperature or relative humidity. For profiles with low LWP the dominant growth process near the surface was aggregation, while in high-LWP conditions the accretion of ice mass due to riming was evident. The ability to distinguish between microphysical processes through the profile suggests the potential for using multiple-frequency and Doppler radars to estimate rime mass content and relate it to the budget of supercooled liquid [e.g. *Moisseev et al.*, 2017], as well as to estimate microphysical process rates [e.g. *Mace and Benson*, 2017]. These features were best resolved in retrievals combining dual-frequency and Doppler measurements; however, the onset of riming was also reliably detected with single-frequency radar retrievals, which could be sufficient to provide improved insights into the position of embedded mixed-phase layers within optically thick ice clouds from space.

In the mixed-phase cloud situations in which riming occurs, ground-based lidars are quickly attenuated by liquid water near the surface. Therefore it was not possible in this study to exploit radar–lidar synergy, either for the retrieval of ice [e.g. *Delanoë and Hogan*, 2010] or for a simultaneous estimate of ice and liquid; instead a correction for liquid attenuation was applied to the radar reflectivity, and the retrieval carried out only for ice. LWP estimates from a co-located microwave radiometer were combined with an assumption about the vertical distribution of liquid water to estimate the radar attenuation as a pre-processing step before the radar retrieval. A more satisfactory approach within the optimal estimation

retrieval framework would be to include a microwave radiometer forward model and perform a synergy retrieval, building upon studies into the active and passive microwave scattering of snow [e.g. *Kneifel et al.*, 2010]. This would provide additional constraints on retrievals of cloud and precipitation to those provided by other passive shortwave and longwave radiances [e.g. *Leinonen et al.*, 2016] or path-integrated attenuation from surface radar backscatter [e.g *Haynes et al.*, 2009; *Hawkness-Smith*, 2010].

The CAPTIVATE retrieval has been developed for the synergy of EarthCARE's 94-GHz cloud profiling Doppler radar [*Illingworth et al.*, 2015] with high-spectral resolution atmospheric lidar and multi-spectral imaging radiometer. The capabilities of multiple-frequency Doppler radars—as well as synergies with a range of active and passive measurements including microwave radiometers—are also of interest. In this study we have considered the contribution of Doppler velocity and dual-frequency radars to the optimal estimation of snow, following a previous study using airborne dual-frequency Doppler radars for CAPTIVATE retrievals of tropical rain [*Mason et al.*, 2017]. Retrievals assimilating both dual-frequency and Doppler radar measurements to retrieve two parameters of the ice PSD and the density factor performed best, producing estimates of particle number concentration, size and bulk density near the surface that were close to in situ measurements. A single-frequency Doppler radar was best constrained when retrieving a single parameter of the PSD; however, we demonstrated that such a retrieval was sufficient to diagnose rimed snow in stratiform snow—wherein the mean Doppler velocity can be assumed to be dominated by hydrometeor fallspeed and not vertical air motion—and that the retrieval is robust to large observational uncertainties. The many challenges of making use of Doppler velocity measurements from space—including vertical resolution, horizontal averaging [e.g. *Kollias et al.*, 2014], ground clutter, and radar mispointing [e.g. *Battaglia and Kollias*, 2015]—have not been considered here, and work is ongoing to apply radar simulators to airborne and ground-based measurements or numerical models to better understand the outlook for retrievals from EarthCARE [e.g. *Battaglia and Tanelli*, 2011]. Beyond EarthCARE, the prospect of spaceborne multiple-frequency Doppler radars [*National Academies of Sciences Engineering and Medicine*, 2018] provides opportunities for further advancements in the global remote-sensing of ice, including estimates of the morphology and microphysics of snow and insights into mixed-phase clouds.

Acknowledgments

We thank three anonymous reviewers for motivating significant improvements to this study, and Chris Westbrook for helpful discussions throughout. Alessio Bozzo is thanked for his contribution to the development of the CAPTIVATE software. This work is supported by the National Centre for Earth Observation (NCEO) and European Space Agency Grant 4000112030/15/NL/CT, with computing resources provided by the University of Reading. C. Chiu is funded by the Office of Science (BER), DOE under grant DE-SC0011666. D. Moisseev acknowledges the funding received by ERA-PLANET, trans-national project iCUPE (Grant Agreement no. 689443), funded under the EU Horizon 2020 Framework Programme and Academy of Finland (grants 307331 and 305175). Contributions by S. Kneifel were carried out within the Emmy-Noether Group OPTIMIce funded by the German Science Foundation (DFG) under Grant KN 1112/2-1.

BAECC 2014 radar data are available from the ARM data archive (`www.arm.gov/data`), and PIP particle measurements for two years at Hyytiälä can be accessed at github (`github.com/dmoisseev/Snow-Retrievals-2014-2015`).

References

Battaglia, A., and P. Kollias (2015), Using Ice Clouds for Mitigating the EarthCARE Doppler Radar Mispointing, *IEEE Transactions on Geoscience and Remote Sensing*, *53*(4), 2079–2085, doi:10.1109/TGRS.2014.2353219.

Battaglia, A., and S. Tanelli (2011), DOMUS: DOppler MUltiple-Scattering Simulator, *IEEE Transactions on Geoscience and Remote Sensing*, *49*(1), 442–450, doi:10.1109/TGRS.2010.2052818.

Brown, P. R. A., and P. N. Francis (1995), Improved Measurements of the Ice Water Content in Cirrus Using a Total-Water Probe, *Journal of Atmospheric and Oceanic Technology*, *12*(2), 410–414, doi:10.1175/1520-0426(1995)012<0410:IMOTIW>2.0.CO;2.

Cadeddu, M. P., J. C. Liljegren, and D. D. Turner (2013), The Atmospheric radiation measurement (ARM) program network of microwave radiometers: instrumentation, data, and retrievals, *Atmospheric Measurement Techniques*, *6*(9), 2359–2372, doi:10.5194/amt-6-2359-2013.

Casella, D., G. Panegrossi, P. Sanò, A. C. Marra, S. Dietrich, B. T. Johnson, and M. S. Kulie (2017), Evaluation of the GPM-DPR snowfall detection capability: Comparison with CloudSat-CPR, *Atmospheric Research*, *197*, 64–75, doi:

10.1016/J.ATMOSRES.2017.06.018.

Ceccaldi, M., J. Delanoë, R. J. Hogan, N. L. Pounder, A. Protat, and J. Pelon (2013), From CloudSat-CALIPSO to EarthCare: Evolution of the DARDAR cloud classification and its comparison to airborne radar-lidar observations, *Journal of Geophysical Research: Atmospheres*, *118*(14), 7962–7981, doi:10.1002/jgrd.50579.

Cesana, G., J. E. Kay, H. Chepfer, J. M. English, and G. de Boer (2012), Ubiquitous low-level liquid-containing Arctic clouds: New observations and climate model constraints from CALIPSO-GOCCP, *Geophysical Research Letters*, *39*(20), doi:10.1029/2012GL053385.

Chen, S., Y. Hong, M. Kulie, A. Behrangi, P. M. Stepanian, Q. Cao, Y. You, J. Zhang, J. Hu, and X. Zhang (2016), Comparison of snowfall estimates from the NASA CloudSat Cloud Profiling Radar and NOAA/NSSL Multi-Radar Multi-Sensor System, *Journal of Hydrology*, *541*, 862–872, doi:10.1016/j.jhydrol.2016.07.047.

Delanoë, J., and R. J. Hogan (2010), Combined CloudSat-CALIPSO-MODIS retrievals of the properties of ice clouds, *Journal of Geophysical Research: Atmospheres*, *115*(4), D00H29, doi:10.1029/2009JD012346.

Delanoë, J., A. Protat, J. Testud, D. Bouniol, A. J. Heymsfield, A. Bansemer, P. R. A. Brown, and R. M. Forbes (2005), Statistical properties of the normalized ice particle size distribution, *Journal of Geophysical Research*, *110*(D10), D10,201, doi:10.1029/2004JD005405.

Delanoë, J. M. E., and R. J. Hogan (2008), A variational scheme for retrieving ice cloud properties from combined radar, lidar, and infrared radiometer, *Journal of Geophysical Research*, *113*(D7), D07,204, doi:10.1029/2007JD009000.

Delanoë, J. M. E., A. J. Heymsfield, A. Protat, A. Bansemer, and R. J. Hogan (2014), Normalized particle size distribution for remote sensing application, *Journal of Geophysical Research: Atmospheres*, *119*(7), 4204–4227, doi:10.1002/2013JD020700.

Erfani, E., and D. L. Mitchell (2017), Growth of ice particle mass and projected area during riming, *Atmospheric Chemistry and Physics*, *17*(2), 1241–1257, doi:10.5194/acp-17-1241-2017.

Field, P. R., and A. J. Heymsfield (2015), Importance of snow to global precipitation, *Geophysical Research Letters*, *42*(21), doi:10.1002/2015GL065497.

Field, P. R., R. J. Hogan, P. R. A. Brown, A. J. Illingworth, T. W. Choularton, and R. J. Cotton (2005), Parametrization of ice-particle size distributions for mid-latitude stratiform cloud, *Quarterly Journal of the Royal Meteorological Society*, *131*(609), 1997–2017, doi:

10.1256/qj.04.134.

Field, P. R., A. J. Heymsfield, and A. Bansemer (2007), Snow Size Distribution Parameterization for Midlatitude and Tropical Ice Clouds, *Journal of the Atmospheric Sciences*, *64*(12), 4346–4365, doi:10.1175/2007JAS2344.1.

Francis, P. N., P. Hignett, and A. Macke (1998), The retrieval of cirrus cloud properties from aircraft multi-spectral reflectance measurements during EUCREX'93, *Quarterly Journal of the Royal Meteorological Society*, *124*(548), 1273–1291, doi:10.1002/qj.49712454812.

Fujiyoshi, Y., and G. Wakahama (1985), On Snow Particles Comprising an Aggregate, *Journal of the Atmospheric Sciences*, *42*(15), 1667–1674, doi:10.1175/1520-0469(1985)042<1667:OSPCAA>2.0.CO;2.

Grazioli, J., G. Lloyd, L. Panziera, C. R. Hoyle, P. J. Connolly, J. Henneberger, and A. Berne (2015), Polarimetric radar and in situ observations of riming and snowfall microphysics during CLACE 2014, *Atmospheric Chemistry and Physics*, *15*(23), 13,787–13,802, doi:10.5194/acp-15-13787-2015.

Grecu, M., W. S. Olson, S. J. Munchak, S. Ringerud, L. Liao, Z. Haddad, B. L. Kelley, and S. F. McLaughlin (2016), The GPM Combined Algorithm, *Journal of Atmospheric and Oceanic Technology*, *33*(10), 2225–2245, doi:10.1175/JTECH-D-16-0019.1.

Harimaya, T., and M. Sato (1989), Measurement of the Riming Amount on Snowflakes, *Journal of the Faculty of Science, Hokkaido University. Series 7, Geophysics*, *8*(4), 355–366.

Hawkness-Smith, L. (2010), A novel retrieval of liquid water path and a evaluation of the representation of drizzle in numerical models, Ph.D. thesis, University of Reading.

Haynes, J. M., T. S. L'Ecuyer, G. L. Stephens, S. D. Miller, C. Mitrescu, N. B. Wood, and S. Tanelli (2009), Rainfall retrieval over the ocean with spaceborne W-band radar, *Journal of Geophysical Research*, *114*, D00A22, doi:10.1029/2008JD009973.

Helmus, J. J., and S. M. Collis (2016), The Python ARM Radar Toolkit (Py-ART), a Library for Working with Weather Radar Data in the Python Programming Language, *Journal of Open Research Software*, *4*(1), doi:10.5334/jors.119.

Heymsfield, A. J. (1982), A Comparative Study of the Rates of Development of Potential Graupel and Hail Embryos in High Plains Storms, *Journal of the Atmospheric Sciences*, *39*(12), 2867–2897, doi:10.1175/1520-0469(1982)039<2867:ACSOTR>2.0.CO;2.

Heymsfield, A. J., and M. Kajikawa (1987), An Improved Approach to Calculating Terminal Velocities of Plate-like Crystals and Graupel, *Journal of the Atmospheric Sciences*, *44*(7),

1088–1099, doi:10.1175/1520-0469(1987)044<1088:AIATCT>2.0.CO;2.

Heymsfield, A. J., and L. M. Miloshevich (2003), Parameterizations for the Cross-Sectional Area and Extinction of Cirrus and Stratiform Ice Cloud Particles, *Journal of the Atmospheric Sciences*, *60*(7), 936–956, doi:10.1175/1520-0469(2003)060<0936:PFTCSA>2.0.CO;2.

Heymsfield, A. J., and C. D. Westbrook (2010), Advances in the Estimation of Ice Particle Fall Speeds Using Laboratory and Field Measurements, *Journal of the Atmospheric Sciences*, *67*(8), 2469–2482, doi:10.1175/2010JAS3379.1.

Heymsfield, A. J., C. Schmitt, A. Bansemer, and C. H. Twohy (2010), Improved Representation of Ice Particle Masses Based on Observations in Natural Clouds, *Journal of the Atmospheric Sciences*, *67*(10), 3303–3318, doi:10.1175/2010JAS3507.1.

Heymsfield, A. J., S. Y. Matrosov, and N. B. Wood (2016), Toward Improving Ice Water Content and Snow-Rate Retrievals from Radars. Part I: X and W Bands, Emphasizing CloudSat, *Journal of Applied Meteorology and Climatology*, *55*(9), 2063–2090, doi:10.1175/JAMC-D-15-0290.1.

Hiley, M. J., M. S. Kulie, and R. Bennartz (2011), Uncertainty Analysis for CloudSat Snowfall Retrievals, *Journal of Applied Meteorology and Climatology*, *50*(2), 399–418, doi:10.1175/2010JAMC2505.1.

Hogan, R. J. (2007), A Variational Scheme for Retrieving Rainfall Rate and Hail Reflectivity Fraction from Polarization Radar, *Journal of Applied Meteorology and Climatology*, *46*(10), 1544–1564, doi:10.1175/JAM2550.1.

Hogan, R. J. (2008), Fast Lidar and Radar Multiple-Scattering Models. Part I: Small-Angle Scattering Using the Photon VarianceâĂŞCovariance Method, *Journal of the Atmospheric Sciences*, *65*(12), 3621–3635, doi:10.1175/2008JAS2642.1.

Hogan, R. J. (2014), Fast Reverse-Mode Automatic Differentiation using Expression Templates in C++, *ACM Transactions on Mathematical Software*, *40*(4), 1–16, doi:10.1145/2560359.

Hogan, R. J. (2017), Adept 2.0: a combined automatic differentiation and array library for C++, doi:10.5281/ZENODO.1004730.

Hogan, R. J., and A. J. Illingworth (1999), The Potential of Spaceborne Dual-Wavelength Radar to Make Global Measurements of Cirrus Clouds, *Journal of Atmospheric and Oceanic Technology*, *16*(5), 518–531, doi:10.1175/1520-0426(1999)016<0518:TPOSDW>2.0.CO;2.

Hogan, R. J., and C. D. Westbrook (2014), Equation for the Microwave Backscatter Cross Section of Aggregate Snowflakes Using the Self-Similar Rayleigh-Gans Approximation, *Journal of the Atmospheric Sciences*, *71*(9), 3292–3301, doi:10.1175/JAS-D-13-0347.1.

Hogan, R. J., P. N. Francis, H. Flentje, A. J. Illingworth, M. Quante, and J. Pelon (2003), Characteristics of mixed-phase clouds. I: Lidar, radar and aircraft observations from CLARE'98, *Quarterly Journal of the Royal Meteorological Society*, *129*(592), 2089–2116, doi:10.1256/rj.01.208.

Hogan, R. J., M. D. Behera, E. J. O'Connor, and A. J. Illingworth (2004), Estimate of the global distribution of stratiform supercooled liquid water clouds using the LITE lidar, *Geophysical Research Letters*, *31*(5), L05,106, doi:10.1029/2003GL018977.

Hogan, R. J., L. Tian, P. R. A. Brown, C. D. Westbrook, A. J. Heymsfield, and J. D. Eastment (2012), Radar Scattering from Ice Aggregates Using the Horizontally Aligned Oblate Spheroid Approximation, *Journal of Applied Meteorology and Climatology*, *51*(3), 655–671, doi:10.1175/JAMC-D-11-074.1.

Hogan, R. J., R. Honeyager, J. Tyynelä, and S. Kneifel (2017), Calculating the millimetre-wave scattering phase function of snowflakes using the self-similar Rayleigh-Gans Approximation, *Quarterly Journal of the Royal Meteorological Society*, *143*(703), 834–844, doi:10.1002/qj.2968.

Hou, A. Y., R. K. Kakar, S. Neeck, A. A. Azarbarzin, C. D. Kummerow, M. Kojima, R. Oki, K. Nakamura, and T. Iguchi (2014), The Global Precipitation Measurement Mission, *Bulletin of the American Meteorological Society*, *95*(5), 701–722, doi:10.1175/BAMS-D-13-00164.1.

Illingworth, A. J., and T. M. Blackman (2002), The Need to Represent Raindrop Size Spectra as Normalized Gamma Distributions for the Interpretation of Polarization Radar Observations, *Journal of Applied Meteorology*, *41*(3), 286–297, doi:10.1175/1520-0450(2002)041<0286:TNTRRS>2.0.CO;2.

Illingworth, A. J., R. J. Hogan, E. J. O'Connor, D. Bouniol, J. Delanoë, J. Pelon, A. Protat, M. E. Brooks, N. Gaussiat, D. R. Wilson, D. P. Donovan, H. K. Baltink, G.-J. van Zadelhoff, J. D. Eastment, J. W. F. Goddard, C. L. Wrench, M. Haeffelin, O. A. Krasnov, H. W. J. Russchenberg, J.-M. Piriou, F. Vinit, A. Seifert, A. M. Tompkins, and U. Willén (2007), Cloudnet, *Bulletin of the American Meteorological Society*, *88*(6), 883–898, doi:10.1175/BAMS-88-6-883.

1184 Illingworth, A. J., H. W. Barker, A. Beljaars, M. Ceccaldi, H. Chepfer, N. Clerbaux,
1185 J. Cole, J. Delanoë, C. Domenech, D. P. Donovan, S. Fukuda, M. Hirakata, R. J. Hogan,
1186 A. Huenerbein, P. Kollias, T. Kubota, T. Nakajima, T. Y. Nakajima, T. Nishizawa, Y. Ohno,
1187 H. Okamoto, R. Oki, K. Sato, M. Satoh, M. W. Shephard, A. Velázquez-Blázquez,
1188 U. Wandinger, T. Wehr, and G.-J. van Zadelhoff (2015), The EarthCARE Satellite: The
1189 Next Step Forward in Global Measurements of Clouds, Aerosols, Precipitation, and
1190 Radiation, *Bulletin of the American Meteorological Society*, *96*(8), 1311–1332, doi:
1191 10.1175/BAMS-D-12-00227.1.

1192 Jiang, Z., M. Oue, J. Verlinde, E. E. Clothiaux, K. Aydin, G. Botta, and Y. Lu (2017), What
1193 Can We Conclude about the Real Aspect Ratios of Ice Particle Aggregates from Two-
1194 Dimensional Images?, *Journal of Applied Meteorology and Climatology*, *56*(3), 725–734,
1195 doi:10.1175/JAMC-D-16-0248.1.

1196 Jullien, R. (1992), The application of fractals to colloidal aggregation, *Croatica Chemica*
1197 *Acta*, *65*(2), 215–235.

1198 Kalesse, H., W. Szyrmer, S. Kneifel, P. Kollias, and E. Luke (2016), Fingerprints of a riming
1199 event on cloud radar Doppler spectra: observations and modeling, *Atmospheric Chemistry*
1200 *and Physics*, *16*(5), 2997–3012, doi:10.5194/acp-16-2997-2016.

1201 Khvorostyanov, V. I., and J. A. Curry (2005), Fall Velocities of Hydrometeors in the Atmo-
1202 sphere: Refinements to a Continuous Analytical Power Law, *Journal of the Atmospheric*
1203 *Sciences*, *62*(12), 4343–4357, doi:10.1175/JAS3622.1.

1204 Kneifel, S., U. Löhnert, A. Battaglia, S. Crewell, and D. Siebler (2010), Snow scattering sig-
1205 nals in ground-based passive microwave radiometer measurements, *Journal of Geophysi-*
1206 *cal Research*, *115*(D16), D16,214, doi:10.1029/2010JD013856.

1207 Kneifel, S., M. Maahn, G. Peters, and C. Simmer (2011), Observation of snowfall with a
1208 low-power FM-CW K-band radar (Micro Rain Radar), *Meteorology and Atmospheric*
1209 *Physics*, *113*(1-2), 75–87, doi:10.1007/s00703-011-0142-z.

1210 Kneifel, S., A. von Lerber, J. Tiira, D. Moisseev, P. Kollias, and J. Leinonen (2015), Ob-
1211 served relations between snowfall microphysics and triple-frequency radar measure-
1212 ments, *Journal of Geophysical Research: Atmospheres*, *120*(12), 6034–6055, doi:
1213 10.1002/2015JD023156.

1214 Kneifel, S., J. Dias Neto, D. Ori, D. Moisseev, J. Tyynelä, I. S. Adams, K.-S. Kuo, R. Ben-
1215 nartz, A. Berne, E. E. Clothiaux, P. Eriksson, A. J. Geer, R. Honeyager, J. Leinonen, and
1216 C. D. Westbrook (2018), Summer Snowfall Workshop: Scattering Properties of Realis-

tic Frozen Hydrometeors from Simulations and Observations, as well as Defining a New Standard for Scattering Databases, *Bulletin of the American Meteorological Society*, *99*(3), ES55–ES58, doi:10.1175/BAMS-D-17-0208.1.

Kollias, P., S. Tanelli, A. Battaglia, and A. Tatarevic (2014), Evaluation of EarthCARE Cloud Profiling Radar Doppler Velocity Measurements in Particle Sedimentation Regimes, *Journal of Atmospheric and Oceanic Technology*, *31*(2), 366–386, doi:10.1175/JTECH-D-11-00202.1.

Kulie, M. S., and R. Bennartz (2009), Utilizing Spaceborne Radars to Retrieve Dry Snowfall, *Journal of Applied Meteorology and Climatology*, *48*(12), 2564–2580, doi:10.1175/2009JAMC2193.1.

Kulie, M. S., L. Milani, N. B. Wood, S. A. Tushaus, R. Bennartz, and T. S. L'Ecuyer (2016), A Shallow Cumuliform Snowfall Census Using Spaceborne Radar, *Journal of Hydrometeorology*, *17*(4), 1261–1279, doi:10.1175/JHM-D-15-0123.1.

Langleben, M. P. (1954), The terminal velocity of snowflakes, *Quarterly Journal of the Royal Meteorological Society*, *80*(344), 174–181, doi:10.1002/qj.49708034404.

Leinonen, J., and D. Moisseev (2015), What do triple-frequency radar signatures reveal about aggregate snowflakes?, *Journal of Geophysical Research: Atmospheres*, *120*(1), 229–239, doi:10.1002/2014JD022072.

Leinonen, J., and W. Szyrmer (2015), Radar signatures of snowflake riming: A modeling study, *Earth and Space Science*, *2*(8), 346–358, doi:10.1002/2015EA000102.

Leinonen, J., M. D. Lebsock, G. L. Stephens, and K. Suzuki (2016), Improved Retrieval of Cloud Liquid Water from CloudSat and MODIS, *Journal of Applied Meteorology and Climatology*, *55*(8), 1831–1844, doi:10.1175/JAMC-D-16-0077.1.

Li, H., D. Moisseev, and A. von Lerber (2018), How Does Riming Affect Dual-Polarization Radar Observations and Snowflake Shape?, *Journal of Geophysical Research: Atmospheres*, *123*(11), 6070–6081, doi:10.1029/2017JD028186.

Liebe, H. J. (1985), An updated model for millimeter wave propagation in moist air, *Radio Science*, *20*(5), 1069–1089.

Lin, Y., and B. A. Colle (2011), A New Bulk Microphysical Scheme That Includes Riming Intensity and Temperature-Dependent Ice Characteristics, *Monthly Weather Review*, *139*(3), 1013–1035, doi:10.1175/2010MWR3293.1.

Lin, Y., L. J. Donner, and B. A. Colle (2011), Parameterization of Riming Intensity and Its Impact on Ice Fall Speed Using ARM Data, *Monthly Weather Review*, *139*(3), 1036–1047,

1250 doi:10.1175/2010MWR3299.1.

1251 Liu, G. (2008), Deriving snow cloud characteristics from CloudSat observations, *Journal of*
1252 *Geophysical Research*, *113*(D8), D00A09, doi:10.1029/2007JD009766.

1253 Löhnert, U., S. Kneifel, A. Battaglia, M. Hagen, L. Hirsch, and S. Crewell (2011), A Mul-
1254 tisensor Approach Toward a Better Understanding of Snowfall Microphysics: The
1255 TOSCA Project, *Bulletin of the American Meteorological Society*, *92*(5), 613–628, doi:
1256 10.1175/2010BAMS2909.1.

1257 Maahn, M., and U. Löhnert (2017), Potential of Higher-Order Moments and Slopes of the
1258 Radar Doppler Spectrum for Retrieving Microphysical and Kinematic Properties of Arc-
1259 tic Ice Clouds, *Journal of Applied Meteorology and Climatology*, *56*(2), 263–282, doi:
1260 10.1175/JAMC-D-16-0020.1.

1261 Maahn, M., U. Löhnert, P. Kollias, R. C. Jackson, and G. M. McFarquhar (2015), Developing
1262 and Evaluating Ice Cloud Parameterizations for Forward Modeling of Radar Moments
1263 Using in situ Aircraft Observations, *Journal of Atmospheric and Oceanic Technology*,
1264 *32*(5), 880–903, doi:10.1175/JTECH-D-14-00112.1.

1265 Mace, G., and S. Benson (2017), Diagnosing Cloud Microphysical Process Information from
1266 Remote Sensing Measurements—A Feasibility Study Using Aircraft Data. Part I: Tropical
1267 Anvils Measured during TC4, *Journal of Applied Meteorology and Climatology*, *56*(3),
1268 633–649, doi:10.1175/JAMC-D-16-0083.1.

1269 Mason, S. L., J. C. Chiu, R. J. Hogan, and L. Tian (2017), Improved rain-rate and drop-
1270 size retrievals from airborne and spaceborne Doppler radar, *Atmospheric Chemistry and*
1271 *Physics Discussions*, pp. 1–34, doi:10.5194/acp-2017-280.

1272 Mitchell, D. (1996), Use of mass-and area-dimensional power laws for determining precipita-
1273 tion particle terminal velocities, *Journal of the atmospheric sciences*.

1274 Mitchell, D. L., and A. J. Heymsfield (2005), Refinements in the Treatment of Ice Particle
1275 Terminal Velocities, Highlighting Aggregates, *Journal of the Atmospheric Sciences*, *62*(5),
1276 1637–1644, doi:10.1175/JAS3413.1.

1277 Mitchell, D. L., R. Zhang, and R. L. Pitter (1990), Mass-Dimensional Relationships for Ice
1278 Particles and the Influence of Riming on Snowfall Rates, *Journal of Applied Meteorology*,
1279 *29*(2), 153–163, doi:10.1175/1520-0450(1990)029<0153:MDRFIP>2.0.CO;2.

1280 Moisseev, D., A. von Lerber, and J. Tiira (2017), Quantifying the effect of riming on snow-
1281 fall using ground-based observations, *Journal of Geophysical Research: Atmospheres*,
1282 *122*, doi:10.1002/2016JD026272.

Morrison, H., and J. A. Milbrandt (2015), Parameterization of Cloud Microphysics Based on the Prediction of Bulk Ice Particle Properties. Part I: Scheme Description and Idealized Tests, *Journal of the Atmospheric Sciences*, *72*(1), 287–311, doi:10.1175/JAS-D-14-0065.1.

Morrison, H., J. A. Milbrandt, G. H. Bryan, K. Ikeda, S. A. Tessendorf, and G. Thompson (2015), Parameterization of Cloud Microphysics Based on the Prediction of Bulk Ice Particle Properties. Part II: Case Study Comparisons with Observations and Other Schemes, *Journal of the Atmospheric Sciences*, *72*(1), 312–339, doi:10.1175/JAS-D-14-0066.1.

Mosimann, L. (1995), An improved method for determining the degree of snow crystal riming by vertical Doppler radar, *Atmospheric Research*, *37*(4), 305–323, doi:10.1016/0169-8095(94)00050-N.

National Academies of Sciences Engineering and Medicine (2018), *Thriving on Our Changing Planet: A Decadal Strategy for Earth Observation from Space*, National Academies Press, Washington, D.C., doi:10.17226/24938.

Newman, A. J., P. A. Kucera, and L. F. Bliven (2009), Presenting the Snowflake Video Imager (SVI), *Journal of Atmospheric and Oceanic Technology*, *26*(2), 167–179, doi:10.1175/2008JTECHA1148.1.

Palerme, C., J. E. Kay, C. Genthon, T. L'Ecuyer, N. B. Wood, and C. Claud (2014), How much snow falls on the Antarctic ice sheet?, *The Cryosphere*, *8*(4), 1577–1587, doi:10.5194/tc-8-1577-2014.

Petäjä, T., E. J. O'Connor, D. Moisseev, V. A. Sinclair, A. J. Manninen, R. Väänänen, A. von Lerber, J. A. Thornton, K. Nicoll, W. Petersen, V. Chandrasekar, J. N. Smith, P. M. Winkler, O. Krüger, H. Hakola, H. Timonen, D. Brus, T. Laurila, E. Asmi, M.-L. Riekkola, L. Mona, P. Massoli, R. Engelmann, M. Komppula, J. Wang, C. Kuang, J. Bäck, A. Virtanen, J. Levula, M. Ritsche, and N. Hickmon (2016), BAECC: A Field Campaign to Elucidate the Impact of Biogenic Aerosols on Clouds and Climate, *Bulletin of the American Meteorological Society*, *97*(10), 1909–1928, doi:10.1175/BAMS-D-14-00199.1.

Rodgers, C. D. (2000), *Inverse methods for atmospheric sounding: theory and practice*, World Scientific, Singapore.

Schmitt, C. G., and A. J. Heymsfield (2010), The Dimensional Characteristics of Ice Crystal Aggregates from Fractal Geometry, *Journal of the Atmospheric Sciences*, *67*(5), 1605–1616, doi:10.1175/2009JAS3187.1.

Shupe, M. D., P. Kollias, S. Y. Matrosov, and T. L. Schneider (2004), Deriving Mixed-Phase Cloud Properties from Doppler Radar Spectra, *Journal of Atmospheric and Oceanic Technology*, *21*(4), 660–670, doi:10.1175/1520-0426(2004)021<0660:DMCPFD>2.0.CO;2.

Stein, T. H. M., C. D. Westbrook, and J. C. Nicol (2015), Fractal geometry of aggregate snowflakes revealed by triple-wavelength radar measurements, *Geophysical Research Letters*, *42*(1), 176–183, doi:10.1002/2014GL062170.

Stephens, G. L., D. G. Vane, R. J. Boain, G. G. Mace, K. Sassen, Z. Wang, A. J. Illingworth, E. J. O'Connor, W. B. Rossow, S. L. Durden, and others (2002), The CloudSat mission and the A-Train: A new dimension of space-based observations of clouds and precipitation, *Bulletin of the American Meteorological Society*, *83*(12), 1771âĂŞ1790.

Szyrmer, W., and I. Zawadzki (2014), Snow Studies. Part III: Theoretical Derivations for the Ensemble Retrieval of Snow Microphysics from Dual-Wavelength Vertically Pointing Radars, *Journal of the Atmospheric Sciences*, *71*(3), 1158–1170, doi:10.1175/JAS-D-12-0285.1.

Tan, I., T. Storelvmo, and M. D. M. Zelinka (2016), Observational constraints on mixed-phase clouds imply higher climate sensitivity, *Science*, *352*(6282), 224–227, doi:10.1126/science.aad5300.

Tanelli, S., S. L. Durden, E. Im, G. M. Heymsfield, P. Racette, and D. O. Starr (2009), Next-generation spaceborne Cloud Profiling Radars, in *2009 IEEE Radar Conference*, pp. 1–4, IEEE, doi:10.1109/RADAR.2009.4977116.

Testud, J., S. Oury, R. A. Black, P. Amayenc, and X. Dou (2001), The Concept of âĂIJNormalizedâĂİ Distribution to Describe Raindrop Spectra: A Tool for Cloud Physics and Cloud Remote Sensing, *Journal of Applied Meteorology*, *40*(6), 1118–1140, doi:10.1175/1520-0450(2001)040<1118:TCONDT>2.0.CO;2.

Tiira, J., D. N. Moisseev, A. von Lerber, D. Ori, A. Tokay, L. F. Bliven, and W. Petersen (2016), Ensemble mean density and its connection to other microphysical properties of falling snow as observed in Southern Finland, *Atmospheric Measurement Techniques*, *9*(9), 4825–4841, doi:10.5194/amt-9-4825-2016.

Twomey, S. (1977), Introduction to the Mathematics of Inversion in Remote Sensing and Indirect, *Elsevier Scientific Publishing*.

von Lerber, A., D. Moisseev, L. F. Bliven, W. Petersen, A.-M. Harri, and V. Chandrasekar (2017), Microphysical Properties of Snow and Their Link to Ze-S Relations during BAECC 2014, *Journal of Applied Meteorology and Climatology*, *56*(6), 1561–1582, doi:

10.1175/JAMC-D-16-0379.1.

Westbrook, C. D., R. C. Ball, P. R. Field, and A. J. Heymsfield (2004), Theory of growth by differential sedimentation, with application to snowflake formation, *Physical Review E*, *70*(2), 021,403, doi:10.1103/PhysRevE.70.021403.

Yin, M., G. Liu, R. Honeyager, and F. Joseph Turk (2017), Observed differences of triple-frequency radar signatures between snowflakes in stratiform and convective clouds, *Journal of Quantitative Spectroscopy and Radiative Transfer*, *193*, 13–20, doi:10.1016/J.JQSRT.2017.02.017.

Zikmunda, J., and G. Vali (1972), Fall Patterns and Fall Velocities of Rimed Ice Crystals, *Journal of the Atmospheric Sciences*, *29*(7), 1334–1347, doi:10.1175/1520-0469(1972)029<1334:FPAFVO>2.0.CO;2.

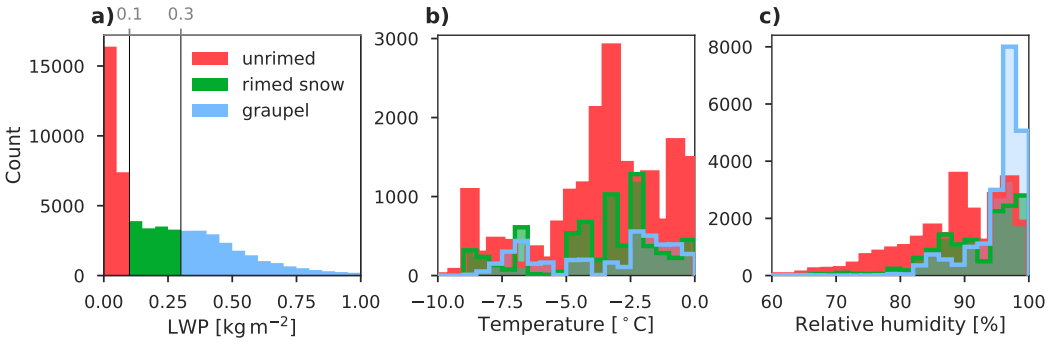

859 **Figure 12.** Histograms of remote-sensed LWP (a) and surface temperature (b) and relative humidity (c)

860 data from all snow events from SNEX IOP, grouped into three LWP classes.

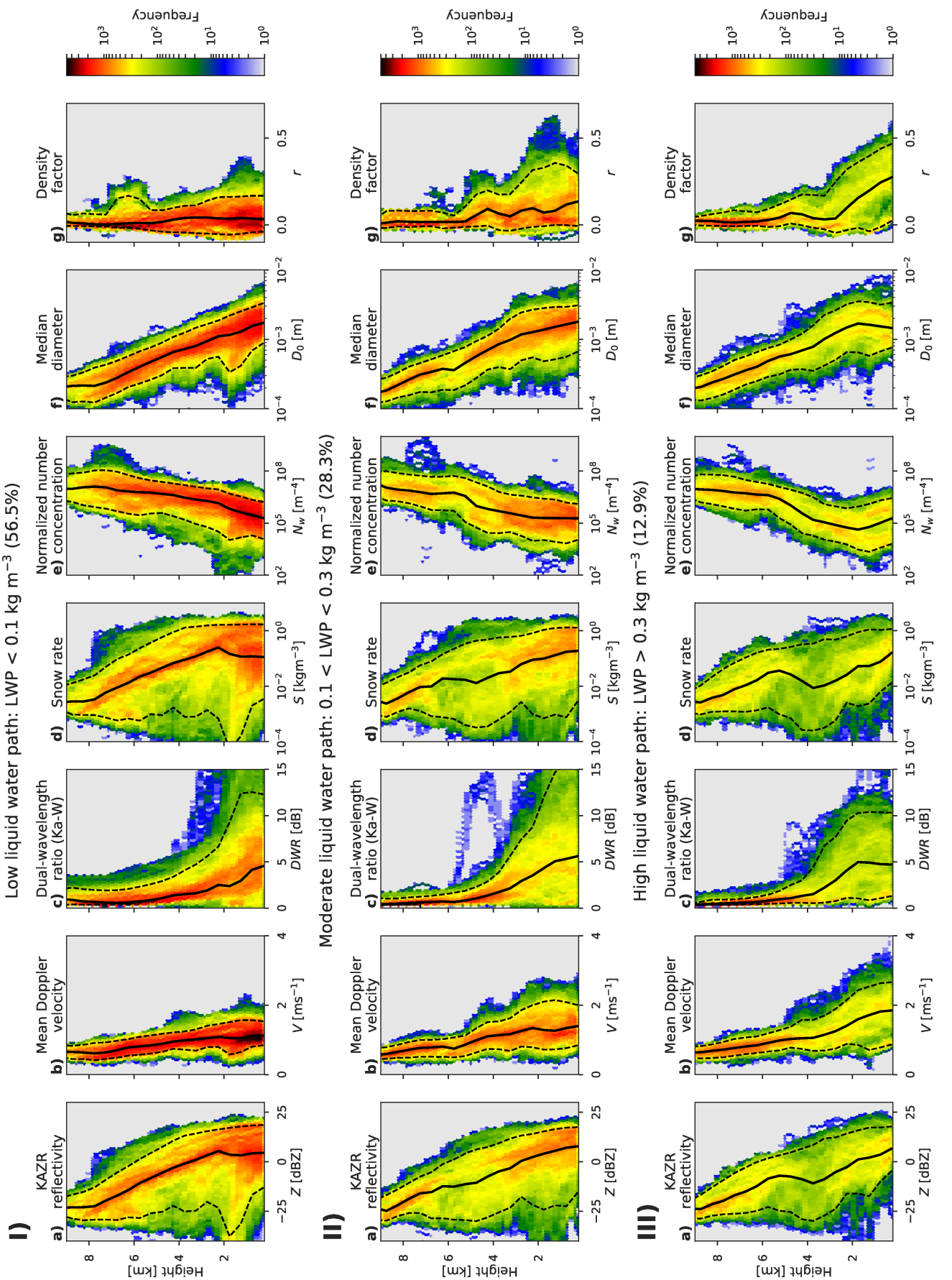

Figure 13. Joint histograms for ZZV$-\alpha_v N_0' r'$ CAPTIVATE retrieval of forward-modelled (a–c) and retrieved (d–g) variables against altitude for snow events during the SNEX 2014 IOP. Snow events are divided into three regimes, unrimed snow (I), rimed snow (II) and graupel (III), using LWP as a proxy for riming. Solid black lines indicate the median—and dashed lines the 5th and 95th percentiles—of the forward modelled or retrieved values at each height.